STEMedicine

Convolutional neural network for disease detection

STEMedicine

stemedicine.org

Multiple sclerosis eetection via 6-layer stochastic pooling convolutional neural network and multiple-way data augmentation

Jian WANG[1][*], Dimas LIMA[2][*]

1 School of Computing and Mathematical Sciences, University of Leicester, Leicester, LE1 7RH, UK
2 Department of Electrical Engineering, Federal University of Santa Catarina, 88040-900, Florianópolis, Brazil

*Correspondence: jw830@le.ac.uk, dimaslima@ieee.org
https://doi.org/10.37175/stemedicine.v2i8.101

ABSTRACT

Background: Multiple sclerosis is one of most widespread autoimmune neuroinflammatory diseases which mainly damages body function such as movement, sensation, and vision. Despite of conventional clinical presentation, brain magnetic resonance imaging of white matter lesions is often applied to diagnose multiple sclerosis at the early stage.

Methods: In this article, we proposed a 6-layer stochastic pooling convolutional neural network (CNN) with multiple-way data augmentation for multiple sclerosis detection in brain magnetic resonance imaging. Our approach does not demand hand-crafted features unlike those traditional machine learning methods. Via application of stochastic pooling and multiple-way data augmentation, our 6-layer CNN achieved equivalent performance against those deep learning methods which consist of so many layers and parameters that ordinarily bring difficulty to training. Further, we also conducted ablation experiments to examine the contribution of stochastic pooling and multiple-way data augmentation to the original CNN model.

Results: The results showed that this 6-layer CNN obtained a sensitivity of 95.98 ± 0.46%, a specificity of 95.67 ± 0.92%, and an accuracy of 95.82 ± 0.58%. According to comparison experiments, our results are better than state-of-the-art approaches.

Conclusion: Our scheme of stochastic pooling and multiple-way data augmentation enhanced the original 6-layer CNN model compared to those using maximum pooling or average pooling and inadequate data augmentation.

Keywords: Multiple sclerosis · Convolutional neural network · Stochastic pooling · Data augmentation · Magnetic resonance imaging

Introduction

Multiple sclerosis (MS) is an autoimmune disease characterized by demyelinating inflammatory white matter lesions of the central nervous system. MS does harm for patient's health by impeding nerve-signal transmitted between brain and other parts of body. It often involves periventricular white matter, spinal cord, brainstem, cerebellum, and optic nerve. Multiple sclerosis may cause loss of muscle coordination, impaired vision, and loss of body function to people. And it is still not clear about its etiology and pathogeneses, which needs further study by medical researchers. Multiple sclerosis can be divided into four categories: (i) relapsing-remitting MS, (ii) secondary-progressive MS, (iii) primary-progressive MS, and (iv) progressive-relapsing MS. Relapsing-remitting MS (R-R) is most commonly observed in clinic, accounting for

around 85% of the total. R-R patients usually endure several times of relapse while in remission period the condition is stable. Secondary-progressive MS (S-P) is derived from R-R gradually. About 80% of R-R patients lead to S-P within twenty-five years and the condition would not be relieved like what it occurs in R-R period. Unlike the R-R and S-P MS, primary-progressive MS (P-P) skips the beginning stage. Patient's condition is aggravated since firstly affected by multiple sclerosis. This category of MS accounts for almost 10% of the total. As for progress-relapsing (P-R) MS, it is rarely seen in clinic. As we can see, R-R and S-P take major proportion of multiple sclerosis. If patients receive effective and suitable treatment in the early stage of MS, it will decrease the chance of turning from R-R to S-P which means patients could suffer less relapse and pain. Therefore, detection for multiple sclerosis as soon as possible is momentous to doctors fighting against multiple sclerosis.

Though researchers realized the significance of diagnosing multiple sclerosis in the early stage, it is not effortless to identify MS from healthy people accurately. In terms of clinical manifestations, multiple sclerosis is similar with other white matter diseases including disseminated encephalomyelitis (ADEM), acute cerebral infarction (ACI) and neuromyelitis optica (NMO). Under this circumstance, researchers had to look for other techniques to improve the success rate of MS diagnosis. Magnetic resonance imaging (MRI) is often utilized for the diagnosis of MS due to its characteristics of less ionizing radiation damage to human body, clear soft tissue imaging quality, and the ability to obtain original three-dimensional cross-sectional images without reconstruction. In the meanwhile, scientists also realized that computer-aided diagnosis was playing an increasingly important role in the field of medical image analysis. The methods applying computer vision and digital image processing to brain MRI have surpassed humans in diagnosing diseases such as Alzheimer's (1), epilepsy (2), Creutzfeldt-Jakob disease (3), and cerebral glioma (4). Therefore, the application of computer vision and digital image processing in craniocerebral MRI to improve the diagnosis rate of multiple sclerosis has become the focus of researchers. For example, Wang, et al. (5) proposed a method for multiple sclerosis detection based on biorthogonal wavelet transform, RBF kernel principal component analysis, and logistic regression. Nayak, et al. (6) presented an approach using discrete wavelet transform and AdaBoost with random forests. Recently, Zhang, et al. (7) applied dropout and parametric ReLU in building convolutional neural network (CNN) for MS identification. Eitel, et al. (8) proposed their CNN-based method for MS detection with layer-wise relevance propagation. Alijamaat, et al. (9) put forward wavelet CNN for MS detection in brain MRI images. Han, et al. (10) used adaptive genetic algorithm (AGA) for MS recognition. Han, et al. (11) employed particle swarm optimization (PSO) for MS recognition. Tang (12) used a five-layer CNN (5l-CNN) for MS detection.

These previous works could be divided into two categories. The first category of methods (5, 6) is based on traditional hand-crafted features. They need to coin specific features manually and it is usually boring and time-consuming. The second category of methods (7-9) is based on deep learning. It is common that they adopted deep neural networks which may contain over fifty layers or even two hundred layers to conduct the classification. These huge neural networks, nevertheless, are hard to train and cost too much computational resources (mainly GPUs) which are expensive for some researchers to afford.

In this study, we proposed an approach based on 6-layer convolutional neural network to identify brain MRI images for diagnosis of multiple sclerosis. Compared with the traditional methods based on manual feature extraction, our approach applies CNN. So it has stronger capability of feature extraction and object classification and also avoid the complicated process of manual feature selection. Compared with the methods based on deep neural network, our model structure has only six layers, instead of dozens or even hundreds of layers. Large networks tend to be time-consuming, laborious, and difficult to reach convergence, and also easy to overfit, while our 6-layer neural network does not have these disadvantages. The second strength of the proposed 6-layer CNN is that it adopts stochastic pooling, which brings better generalization performance compared to those deep neural networks using max pooling. And crucially, we conducted up to sixteen methods of data augmentation. To the best of our knowledge, there is no other previous work in a model of diagnosing MS using so many ways of data augmentation. Our approach has the most diverse and comprehensive methods of data augmentation at present. In general, the proposed approach has the characteristics of simple network architecture, fast training speed and easy convergence. At the same time, due to the application of stochastic pooling and multiple-way data augmentation, this approach achieved competitive results in the detection of multiple sclerosis on brain MRI images.

In the next chapter of the paper, we will first introduce the experiment data and the preprocessing operation for the data set. Data and preprocessing are also vital for building a successful neural network of vision task. In the third chapter, we will present the CNN architecture, stochastic pooling, and multiple-way data augmentation step by step. Then we will show the design of our experiments, including validation and evaluation. In the fourth chapter, we will give discussion of experimental results. It is worth noting that our experimental results contain ablation experimental results to demonstrate how much stochastic pooling and multiple-way data augmentation we applied could boost the performance of a simple CNN in MS diagnosis. Finally, in the fifth chapter, we will provide the summary of this study and put forward some possible improvement directions in the future.

Dataset
Sources

We acquired the same dataset as (7). This dataset totally

(a) MS slice

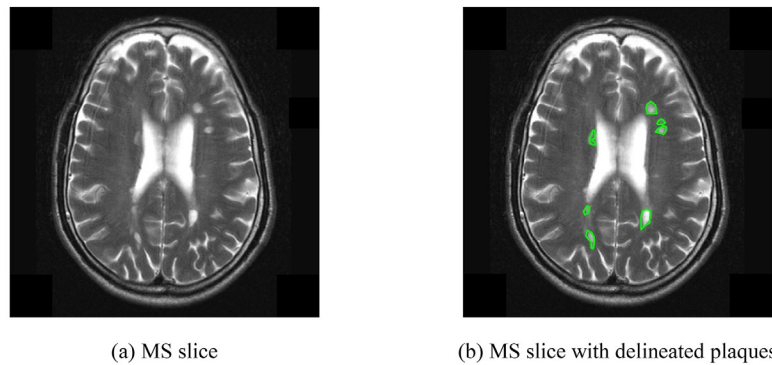(b) MS slice with delineated plaques

Figure 1. Samples of our dataset.

consists of 1357 MRI images in which 676 slices (13) are multiple sclerosis images and 681 slices (7) are health controls. We randomly selected two samples from the dataset as shown in **Figure 1**. **Figure 1** (a) presented one original MS slice and **Figure 1** (b) described the delineated plaques on **Figure 1** (a). We also provided **Table 1** to illustrate the demographic characteristics of the dataset.

Data preprocessing

As we mentioned, our dataset was combined from two sources of images. This would lead to difference of image characteristics between two sources of images on account of factors such as scanning equipment and reconstruction process. In order to restrain the difference, we need to apply contrast normalization technique to balance the two sources of images into a same range of gray-level intensity. In this study, we adopted histogram stretching (14) as our method of contrast normalization because of its effectiveness and simplicity.

The histogram stretching method could be presented as following:

$$\varphi(x,y) = (g(x,y) - g_1)/(g_2 - g_1) \qquad (1)$$

$$g_2 = max(g(x,y)) \qquad (2)$$

$$g_1 = min(g(x,y)) \qquad (3)$$

in which parameters are defined in **Table 2**.

Via this operation, we can observe that the distribution of gray-level intensity in two sources of images are stretched to the same field. As a result, we as far as possible formed the two sources of images into one entire dataset and avoided the negative influence on subsequent process.

Convolutional Neural Network

Pooling Layer

Pooling layer, also named as subsampling or downsampling, is often used behind of convolutional layer in a classic architecture of CNN (15). Its main purposes include reducing feature dimension of convolutional layer output (16), suppressing noise, reducing quantity of parameters and computation cost, and dampening overfitting (17).

Unlike most of other neural network using CNN (18) as backbone, our 6-layer CNN applied stochastic pooling rather than max pooling or average pooling. Suppose there existed a pooling window upon the region of feature map which covered k elements. Each element of feature map was recorded as v_i, and i was the index of element (19). After the pooling window slide upon this region, the output of pooling operation was written as u. Then the max pooling operation could be described as:

$$u = max(v_i) \qquad (4)$$

which means max pooling always selects the biggest element within a region of feature map (20). The average pooling operation could be described as:

$$u = (\Sigma v_i)/k \qquad (5)$$

which means average pooling adopts the mean value of k elements. In stochastic pooling, we first calculated the probability map of the chosen region.

$$p_i = v_i/\Sigma v_i \qquad (6)$$

Then stochastic pooling would choose the value of one element as sampling value according to the probability distribution (21). The p_i was bigger, v_i was more likely chosen as the sampling value, but not definitely. The mechanism could be described as:

$$u = v_i, i\sim P(p_1,\ldots,p_i,..,p_k) \qquad (7)$$

Figure 2 illustrated the comparison between max pooling,

Table 1. Demographic characteristics of the dataset.

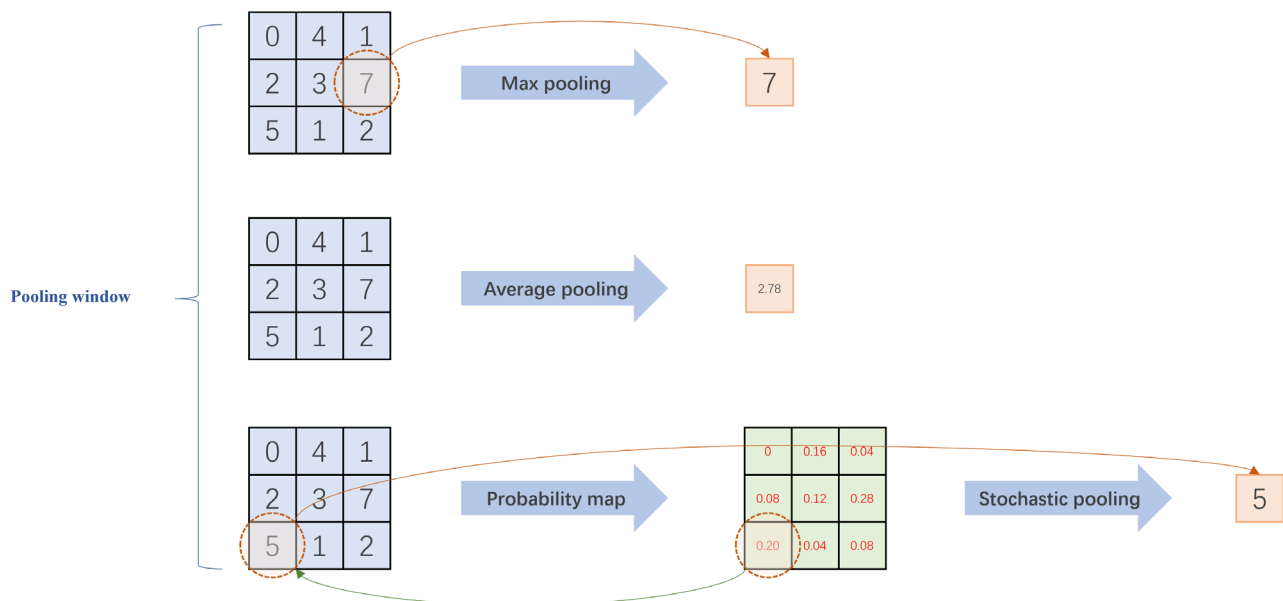| Dataset	Source	Slices	Subjects	Male/Female	Age
Health controls [7]	private	681	26	12/14	33.5 ± 8.3
Multiple sclerosis [13]	eHealth	676	38	17/21	34.1 ± 10.5

Figure 2. Comparison of max pooling, average pooling, and stochastic pooling.

average pooling, and stochastic pooling.

Structure of our six-layer CNN

Our proposed CNN structure consisted of three convolutional layers and three fully-connected layers (22). Generally speaking, convolutional layers are meant to extract features while fully-connected layers are used for classification. Each convolutional layer was followed by activation function and a stochastic pooling layer (23, 24). Activation function was applied for nonlinear transformation after convolution calculation. During the procedure of activation function and pooling layer, there exists no learnable weights (25). Hence, we usually do not count them in neural network structure. As it is shown in **Table 3**, three convolutional layers and three stochastic pooling layers formed the 3-layer convolutional network in the structure.

In our 6-layer CNN structure, it contained three fully-connected layers and three dropout layers. Ahead of each fully-connected layer, a dropout layer was inserted to make CNN more robust to training. The retention probabilities of three dropout layers are set as 0.5, 0.5, and 0.5, respectively, by trial-and-error method. **Table 4**

presented the structure of fully-connected layers in our proposed model. At last, we offered **Figure 3** to portray the whole structure of the proposed 6-layer stochastic pooling CNNs.

Multiple-way data augmentation

It is known that the learning process of neural network cannot leave the support of massive data samples. On most occasions, the more training data are fed to neural network, the better model we attain (26, 27). However, in reality, data samples is often insufficient. Lack of samples will not only impair the model to obtain the best performance, but also lead to difficult training and frequent overfitting. Data augmentation (DA) technology (28, 29) is aimed at expanding the original small dataset into a lager one by means of digital signal processing, so as to alleviate the problem of insufficient samples. In previous work, data augmentation has been applied but with only five ways (rotation, scaling, Gaussian noise, random translation, and Gamma correction) (30). It is our contribution that we exploited up to 18-way data augmentation methods. As far as we are aware, this study applied most ways of data augmentation among existing

Table 2. Parameters in histogram stretching.

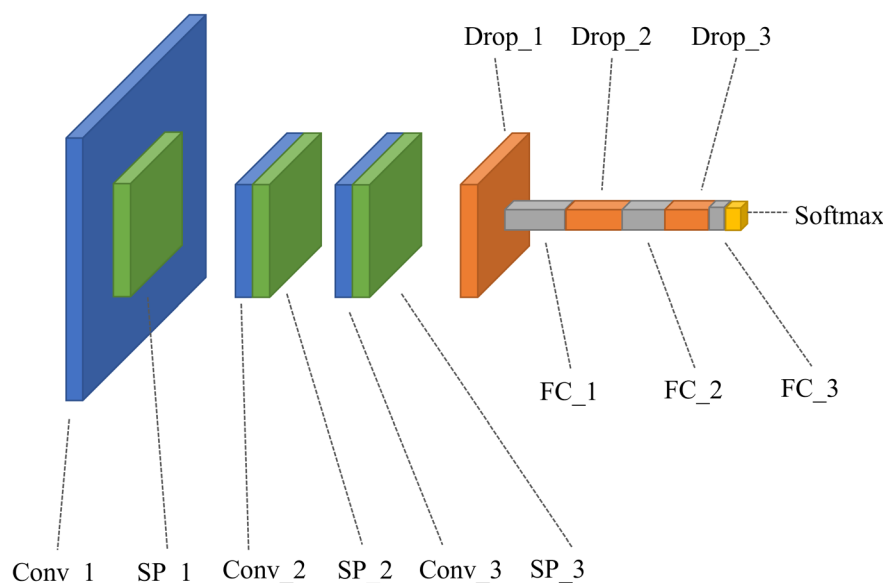| Parameter	Meaning
x	Horizontal coordinate in an image
y	Vertical coordinate in an image
$g(x,y)$	The original gray-level intensity in location (x,y)
g_2	The highest gray-level intensity in an image
g_1	The lowest gray-level intensity in an image
$\varphi(x,y)$	The stretched gray-level intensity in location (x,y)

Figure 3. Structure of 6-layer stochastic pooling CNN.

CNN-based MS detection approaches (31). Our data augmentation methods contained three categories that were geometric-based methods, noise-based methods, and photometric-based methods. At first, there were nine ways of data augmentation (32). Then via reflecting these augmented samples horizontally, we got double sets of data augmentation methods which contained twenty ways in total. **Table 5** provided a list of data augmentation methods we used.

Geometric-based methods

In geometry, geometric-based methods are also named

as affine transformation, which indicates transforming one existing vector space to another one (33). Affine transformation is combined with a linear transformation plus a shift (34). Assume an original vector space was recorded as $\vec{v}$, and the linear transformation could be described as a matrix written as A, meanwhile the shift was written as $\vec{b}$. Then the new transformed vector space $\vec{u}$ was calculated as below.

$$\vec{u} = A\vec{v} + \vec{b} \qquad (8)$$

Back to digital image processing, affine transformation means transform points in the image from their previous

Table 3. Convolutional layers.

Layer	Filter size	Channel	Filters	Stride
Conv_1	7×7	1	1	2
SP_1	3×3			2
Conv_2	3×3	16	16	2
SP_2	3×3			1
Conv_3	3×3	32	32	2
SP_3	3×3			1

Table 4. Fully-connected layers.

Layer	Weights	Bias	Probability
Drop_1			0.5
FC_1	200×16384	200×1	
Drop_2			0.5
FC_2	100×200	100×1	
Drop_3			0.5
FC_3	2×100	2×1	

(a) Horizontal shear

(b) Vertical shear

(c) Rotation

(d) Scaling

(e) Random translation

(f) Gaussian noise

(g) Salt-and-pepper noise

(h) Speckle noise

(i) Gamma correction

Figure 4. Data augmentation results.

coordinates to new ones. Assume the coordinates of the raw image were recorded as $\begin{bmatrix} x \\ y \\ 1 \end{bmatrix}$, and the transformed coordinates were written as $\begin{bmatrix} x' \\ y' \\ 1 \end{bmatrix}$. Then the transformation process could be described as:

$$\begin{bmatrix} x' \\ y' \\ 1 \end{bmatrix} = \begin{bmatrix} A & \vec{b} \\ 0 \quad 0 & 1 \end{bmatrix} \begin{bmatrix} x \\ y \\ 1 \end{bmatrix} \qquad (9)$$

in which $\begin{bmatrix} A & \vec{b} \\ 0 \quad 0 & 1 \end{bmatrix}$ was called affine transformation matrix and was also frequently written as $\begin{bmatrix} a & b & c \\ d & e & f \\ 0 & 0 & 1 \end{bmatrix}$.
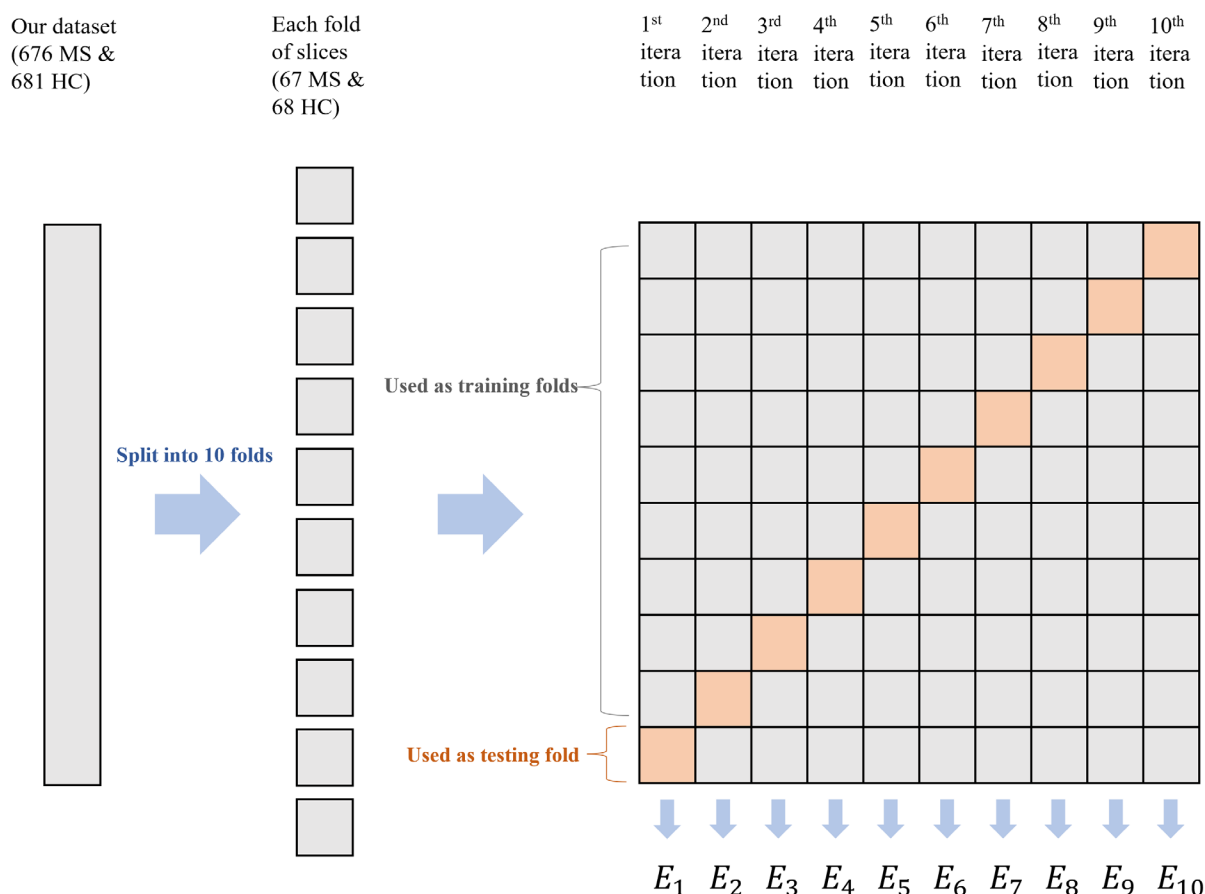
Figure 5. 10-fold cross validation.

Every affine transformation can be represented through particular affine transformation matrix. Here we introduce six ways of affine transformation that employed in this study.

Horizontal flipping. It is a geometric transformation operation performing on the raw image to generate a mirror image which is symmetrical about y-axis (35). Compared to vertical flipping, horizontal flipping is more often adopted and has been tested effectiveness on popular datasets such as ImageNet and CIFAR-10 (36). The affine transformation matrix of horizontal flipping could be written as $\begin{bmatrix} x' \\ y' \\ 1 \end{bmatrix} = \begin{bmatrix} -1 & 0 & 0 \\ 0 & 1 & 0 \\ 0 & 0 & 1 \end{bmatrix}\begin{bmatrix} x \\ y \\ 1 \end{bmatrix}$. Thus, we get the transformed coordinates as follows.

$$\begin{bmatrix} x' \\ y' \\ 1 \end{bmatrix} = \begin{bmatrix} -1 & 0 & 0 \\ 0 & 1 & 0 \\ 0 & 0 & 1 \end{bmatrix}\begin{bmatrix} x \\ y \\ 1 \end{bmatrix} \qquad (10)$$

Horizontal shear. It is defined as changing location of each point in the image horizontally, along the x-axis. And the amount of displacement along the x-axis is determined by each point's coordinate of y-axis (37). The affine transformation matrix of horizontal shear could be written as $\begin{bmatrix} 1 & \tan\alpha & 0 \\ 0 & 1 & 0 \\ 0 & 0 & 1 \end{bmatrix}$. So we attain the transformed

coordinates as below.

$$\begin{bmatrix} x' \\ y' \\ 1 \end{bmatrix} = \begin{bmatrix} 1 & \tan\alpha & 0 \\ 0 & 1 & 0 \\ 0 & 0 & 1 \end{bmatrix}\begin{bmatrix} x \\ y \\ 1 \end{bmatrix} \qquad (11)$$

Figure 4 (a) showed examples of horizontal shear.

Vertical shear. In contrast to horizontal shear, vertical shear is defined as changing location of each point in the image vertically, along the y-axis. And the amount of displacement along the y-axis is determined by each point's coordinate of x-axis. The affine transformation matrix of vertical shear could be written as $\begin{bmatrix} 1 & 0 & 0 \\ \tan\alpha & 1 & 0 \\ 0 & 0 & 1 \end{bmatrix}$ Therefore, we obtain the transformed coordinates as follows.

$$\begin{bmatrix} x' \\ y' \\ 1 \end{bmatrix} = \begin{bmatrix} 1 & 0 & 0 \\ \tan\alpha & 1 & 0 \\ 0 & 0 & 1 \end{bmatrix}\begin{bmatrix} x \\ y \\ 1 \end{bmatrix} \qquad (12)$$

Figure 4 (b) showed examples of vertical shear.

Rotation. Like its name, it rotates an image around a fixed point. In most cases, rotation is around the central point of the image in data augmentation. The affine transformation matrix of rotation could be written as
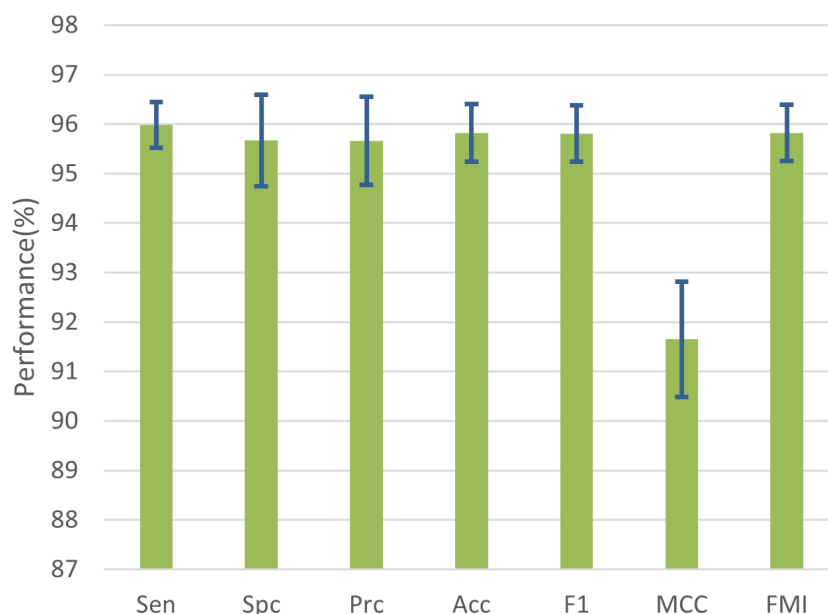
Figure 6. Error bar of stochastic pooling results.

$\begin{bmatrix} 1 & 0 & c \\ 0 & 1 & f \\ 0 & 0 & 1 \end{bmatrix}$. Then the transformation operation could be described as below.

$$\begin{bmatrix} x' \\ y' \\ 1 \end{bmatrix} = \begin{bmatrix} 1 & 0 & c \\ 0 & 1 & f \\ 0 & 0 & 1 \end{bmatrix} \begin{bmatrix} x \\ y \\ 1 \end{bmatrix} \qquad (15)$$

Figure 4 (e) showed examples of random translation.

Noise-based methods

In data augmentation, noise-based methods are defined as injecting noise to image samples. Via adding noise into images, training dataset would enhance its sampling variance so as to overcome the lack of data.

Gaussian noise. As one the most commonly-used noises, Gaussian noise is often added to raw images in data augmentation. Mark z as the gray level, z obeys the probability density function as follow:

$$p(z) = \frac{1}{\sqrt{2\pi}\sigma} e^{-(z-u)^2/2\sigma^2} \qquad (16)$$

where μ represents the mean gray value, and σ means standard deviation of z. **Figure 4** (f) showed examples of Gaussian noise.

Salt-and-pepper noise. It is a widely-used noise in data augmentation as well. In salt-and-pepper noise augmentation, z obeys the probability density function which could be depicted as:

$$p(z) = \begin{cases} P_a & z = a \\ P_b & z = b \\ 0 & otherwise \end{cases} \qquad (17)$$

where a and b are threshold values for salt noise and pepper noise. **Figure 4** (g) showed examples of salt-and-pepper noise.

Speckle noise. As a granular interference, speckle noise naturally occurs in radar or ultrasound images. Suppose F was the observed image, f was the image without noise, N_m referred to multiplicative noise, and N_a referred to additive noise. Then speckle noise could be defined as follows.

$$F = f + N_m f + N_a \qquad (18)$$

Figure 4(h) showed examples of speckle noise.

Photometric-based method

Gamma correction. In the beginning, Gamma correction was made for luminance adjustment in imaging or display system (38). Because human's perception of luminance is not linear with light power, but with a relation of power function. And the exponent of this power function was recorded as γ. The gamma correction is usually written as follows.

$$v_{out} = Av_{in}^{\gamma} \qquad (19)$$

In this equation, v_{out} represents output gray value and v_{in} represents input gray value. When $\gamma < 1$, we often regard this gamma correction as gamma compression. While $\gamma > 1$, we regard it as gamma expansion (39). In this study, we applied gamma correction on raw images of datasets as one of data augmentation methods to enlarge our training samples. **Figure 4** (i) showed examples of Gamma correction.

In the end we provided **Figure 4** to illustrate effects of multiple-way data augmentation.

10-fold Cross Validation

In this study, we utilized 10-fold cross validation as our method of dataset division. We divided the whole dataset into ten folds (40). Each fold contains 67 multiple
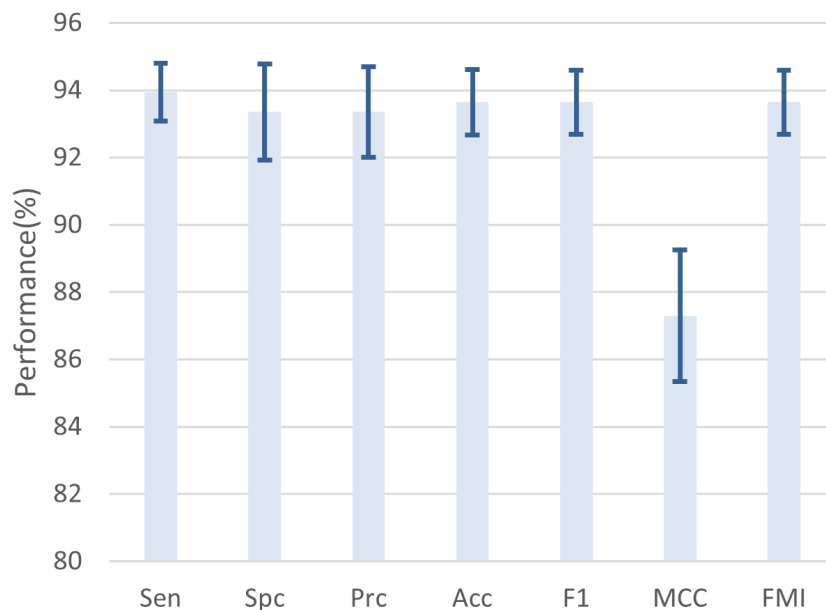
Figure 7. Error bar of average pooling results.

sclerosis slices and 68 health controls. In every iteration, we adopted nine folds of data as training set while the other one fold as testing set and repeated this procedure ten times. **Figure 5** described this process of splitting the dataset into ten folds and repeating training-testing for ten iterations.

In the end, we obtained ten expectations of model performance and calculated the final expectation by averaging the expectations of each iteration (41). This calculation could be written as below:

$$E = \frac{1}{10} \sum_{i=1}^{10} E_i \qquad (20)$$

Measure

In this study, we applied confusion matrix (shown in **Table 6**) to measure the performance.
In confusion matrix, we counted true positive (TP), true negative (TN), false positive (FP), and false negative (FN) and used these values to calculate sensitivity (SEN), specificity (SPC), precision (PRC), accuracy (ACC), F_1 score, Matthews correlation coefficient (MCC), and Fowlkes-Mallows index (FMI). The calculation processes were described as below:

$$SEN = \frac{TP}{TP + FN} \qquad (21)$$

$$SPC = \frac{TN}{TN + FP} \qquad (22)$$

$$PRC = \frac{TP}{TP + FP} \qquad (23)$$

$$ACC = \frac{TP + TN}{TP + TN + FP + FN} \qquad (24)$$

$$F_1 = \frac{2PRC * SEN}{PRC + SEN} \qquad (25)$$

$$MCC = \frac{TP \times TN - FP \times FN}{\sqrt{(TP + FP)(TP + FN)(TN + FP)(TN + FN)}} \qquad (26)$$

$$FMI = \frac{TP}{\sqrt{(TP + FP)(TP + FN)}} \qquad (27)$$

In addition to original measures of sensitivity, specificity, precision, accuracy, F_1 score, MCC, and FMI, we calculated the standard deviation and the average based on these seven measures for further performance comparison experiments as well.

Results and Discussions
Statistical Analysis

Table 7 showed the results of 10 runs. Our approach based on 6-layer stochastic pooling CNNs and multiple-way data augmentation secured a sensitivity of 95.98 ± 0.46%, a specificity of 95.67 ± 0.92%, a precision of 95.66 ± 0.89%, an accuracy of 95.82 ± 0.58%, a F1 score of 95.81 ± 0.57%, a MCC of 91.65 ± 1.16%, and a FMI of 95.82 ± 0.57%. Also, we gave **Figure 6** to present the error bar of 10-run results.

Pooling Methods Comparison

In order to inspect into the contribution stochastic pooling made on the model's performance, we conducted comparison experiments which replaced stochastic pooling with average pooling and max pooling respectively in proposed CNNs. As we can see in **Table 8**, our 6-layer CNN achieved a sensitivity of 93.93 ± 0.86%, a specificity of 93.35 ± 1.42%, a precision of 93.35 ± 1.35%, an accuracy of 93.64 ± 0.98%, a F1 score of 93.64

Table 5. 18-way data augmentation.

DA category	Method	Representation
Geometric-based methods		
	Horizontal flipping	$\begin{bmatrix} -1 & 0 & 0 \\ 0 & 1 & 0 \\ 0 & 0 & 1 \end{bmatrix}$
	Horizontal shear	$\begin{bmatrix} 1 & \tan\alpha & 0 \\ 0 & 1 & 0 \\ 0 & 0 & 1 \end{bmatrix}$
	Vertical shear	$\begin{bmatrix} 1 & 0 & 0 \\ \tan\alpha & 1 & 0 \\ 0 & 0 & 1 \end{bmatrix}$
	Rotation	$\begin{bmatrix} \cos\beta & \sin\beta & c \\ -\sin\beta & \cos\beta & f \\ 0 & 0 & 1 \end{bmatrix}$
	Scaling	$\begin{bmatrix} r & 0 & c \\ 0 & r & f \\ 0 & 0 & 1 \end{bmatrix}$
	Random translation	$\begin{bmatrix} 1 & 0 & c \\ 0 & 1 & f \\ 0 & 0 & 1 \end{bmatrix}$
Noise-based methods		
	Gaussian noise	$p(z) = \dfrac{1}{\sqrt{2\pi}\sigma} e^{-(z-u)^2/2\sigma^2}$
	Salt-and-pepper noise	$p(z) = \begin{cases} P_a & z = a \\ P_b & z = b \\ 0 & otherwise \end{cases}$
	Speckle noise	$F = f + N_m f + N_a$
Photometric-based method		
	Gamma correction	$v_{out} = A v_{in}^{\gamma}$

± 0.96%, a MCC of 87.29 ± 1.96%, and a FMI of 93.64 ± 0.96%. And the error bar of results using average pooling was shown in **Figure 7**.

As it was presented in **Table 9**, with max pooling, the proposed CNN obtained a sensitivity of 94.06 ± 1.54%, a specificity of 94.56 ± 1.44%, a precision of 94.54 ± 1.41%, an accuracy of 94.31 ± 1.27%, a F1 score of 94.30 ± 1.29%, a MCC of 88.64 ± 2.54%, and a FMI of 94.30 ± 1.28%. **Figure 8** depicted the error bar of results using max pooling.

Via these comparison experiments, we could observe that using stochastic pooling earned best performance in almost every measure including sensitivity, specificity, precision, accuracy, F1 score, MCC, and FMI. To make it convenient for presenting the advantage of stochastic pooling, we drew **Figure 9**. It revealed that our model achieved improvement of nearly 2% in each measure when applying stochastic pooling compared with results using average pooling or max pooling.

Comparison with State-of-the-art Algorithms

We compared our 6-layer stochastic pooling CNN with state-of-the-art algorithms for multiple sclerosis detection such as AGA (10), PSO (11), and 5l-CNN (12). These three state-of-the-art algorithms were tested with the same dataset as ours. The comparison results was given in **Table 10**.

Table 6. Confusion matrix of binary classification.

		Predicted	
		Positive	Negative
Actual	Positive	TP	FN
	Negative	FP	TN
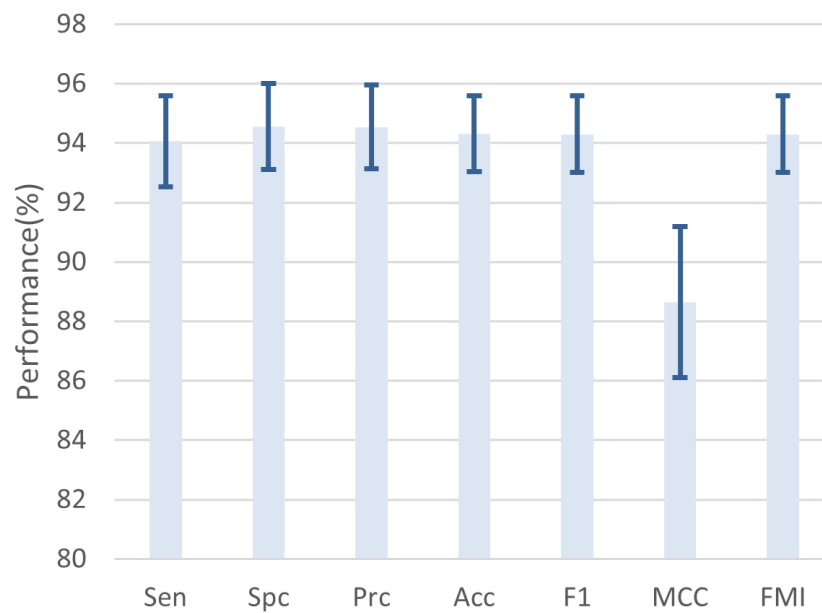
Figure 8. Error bar of max pooling results.

Table 7. Results of ten runs.

Run	Sen	Spc	Prc	Acc	F1	MCC	FMI
1	95.86	95.45	95.43	95.65	95.65	91.31	95.65
2	96.60	96.77	96.74	96.68	96.67	93.37	96.67
3	95.71	96.33	96.28	96.02	95.99	92.04	95.99
4	95.41	95.59	95.56	95.50	95.48	91.01	95.48
5	96.89	95.89	95.90	96.39	96.39	92.78	96.40
6	96.15	96.92	96.87	96.54	96.51	93.08	96.51
7	95.56	96.04	96.99	95.80	95.77	91.60	95.77
8	96.01	94.42	94.47	95.21	95.23	90.43	95.23
9	95.86	95.15	95.15	95.50	95.50	91.01	95.51
10	95.71	94.13	94.18	94.92	94.94	89.84	94.94
MSD	95.98 ± 0.46	95.67 ± 0.92	95.66 ± 0.89	95.82 ± 0.58	95.81 ± 0.57	91.65 ± 1.16	95.82 ± 0.57

Table 8. Experimental results using average pooling.

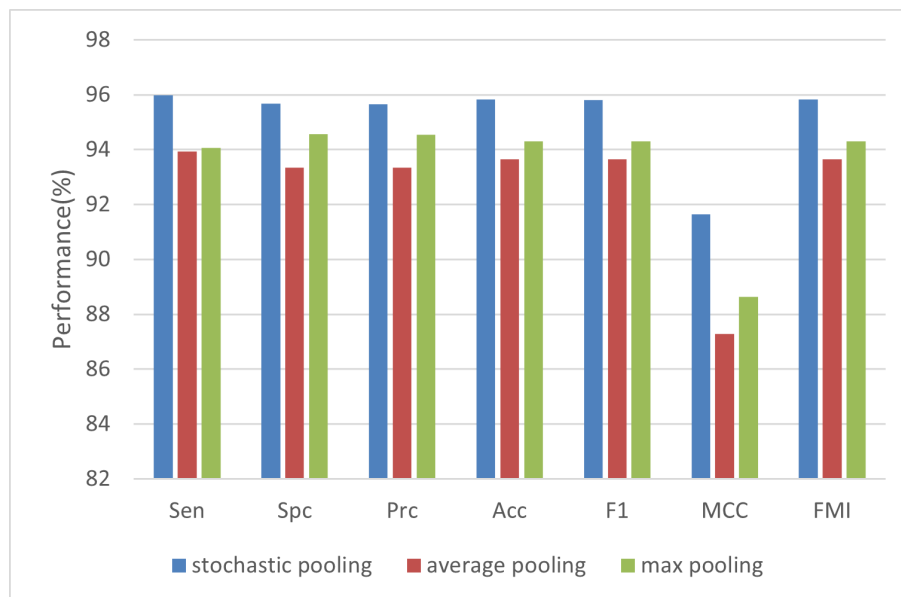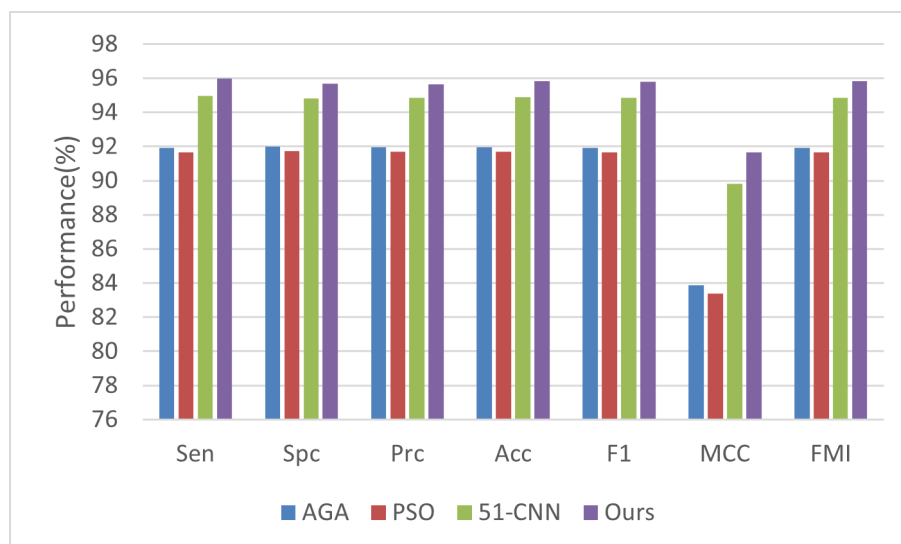| Run	Sen	Spc	Prc	Acc	F1	MCC	FMI
1	93.05	92.51	92.50	92.78	92.77	85.56	92.77
2	95.27	94.27	94.29	94.77	94.78	89.54	94.78
3	93.05	92.95	92.91	93.00	92.98	86.00	92.98
4	92.90	94.13	94.01	93.52	93.45	87.04	93.45
5	94.08	91.63	91.77	92.85	92.91	85.73	92.92
6	94.38	91.92	92.06	93.15	93.21	86.32	93.21
7	93.34	91.63	91.72	92.48	92.52	84.98	92.53
8	95.12	95.45	95.40	95.28	95.26	90.57	95.26
9	94.38	95.15	95.08	94.77	94.73	89.54	94.73
10	93.79	93.83	93.79	93.81	93.79	87.62	93.79
MSD	93.93 ± 0.86	93.35 ± 1.42	93.35 ± 1.35	93.64 ± 0.98	93.64 ± 0.96	87.29 ± 1.96	93.64 ± 0.96

Figure 9. Pooling methods comparison.

Figure 10. Comparison plot.

Table 9. Experimental results using max pooling.

Run	Sen	Spc	Prc	Acc	F1	MCC	FMI
1	95.00	94.69	94.70	94.84	94.85	89.69	94.85
2	95.00	95.00	95.00	95.00	95.00	90.00	95.00
3	93.12	95.31	95.21	94.22	94.15	88.46	94.16
4	94.69	95.62	95.58	95.16	95.13	90.32	95.13
5	95.31	96.88	96.83	96.09	96.06	92.20	96.07
6	95.31	95.94	95.91	95.62	95.61	91.25	95.61
7	95.31	92.50	92.71	93.91	93.99	87.85	94.00
8	93.12	93.12	93.12	93.12	93.12	86.25	93.12
9	93.12	93.12	93.12	93.12	93.12	86.25	93.12
10	90.62	93.44	93.25	92.03	91.92	84.10	91.93
MSD	94.06 ± 1.54	94.56 ± 1.44	94.54 ± 1.41	94.31 ± 1.27	94.30 ± 1.29	88.64 ± 2.54	94.30 ± 1.28

Table 10. Comparison with SOTA.

Method	Sen	Spc	Prc	Acc	F1	MCC	FMI
AGA [10]	91.91 ± 1.24	91.98 ± 1.36	91.97 ± 1.32	91.95 ± 1.19	91.92 ± 1.20	83.89 ± 2.41	91.92 ± 1.19
PSO [11]	91.67 ± 1.41	91.73 ± 0.77	91.70 ±0 .78	91.70 ± 0.97	91.67 ± 1.00	83.40 ± 1.98	91.67 ± 0.99
5l-CNN [12]	94.96 ± 1.43	94.82 ± 1.67	94.85 ± 1.62	94.89 ± 1.37	94.87 ± 1.37	89.83 ± 2.74	94.87 ± 1.37
Ours	95.98±0.46	95.67 ± 0.92	95.66 ± 0.89	95.82 ± 0.58	95.81 ± 0.57	91.65 ± 1.16	95.82 ± 0.57

We also offered **Figure 10** to show our method's strength against state-of-the-art algorithms. We could observe that our proposed method acquired the best sensitivity, specificity, accuracy, F1 score, MCC, and FMI, surpassing the second-best algorithm by nearly 1% in every measure. Besides, our method gained the least standard deviation compared state-of-the-art algorithms. These results showed the effectiveness of our proposed approach.

There are some shortcomings of our proposed approach: (i) The dataset we used in this study is not abundant. We will seek for bigger datasets or collecting more sample images. (ii) We will try some new deep learning technologies in multiple sclerosis detection such as attention mechanism.

Conclusions

In this study, we proposed a novel framework for multiple sclerosis detection using 6-layer stochastic pooling CNN combined with multiple-way data augmentation. We added stochastic pooling in our framework and tested its superiority to other pooling methods via comparison experiments. We also proposed 18-way data augmentation methods including geometric-based methods, noise-based methods, and photometric-based methods. Our approach beat several state-of-the-art algorithms, attaining a sensitivity of 95.98 ± 0.46%, a specificity of 95.67 ± 0.92%, a precision of 95.66 ± 0.89%, an accuracy of 95.82 ± 0.58%, and a F1 score of 95.81 ± 0.57%. The experimental results showed that our approach achieved highest performance in multiple sclerosis detection compared to several state-state-of-the-art algorithms.

Conflict of interest
The authors declare that they have no conflicts of interest to disclose.

References
1. Dua M, Makhija D, Manasa PYL, Mishra P. A CNN–RNN–LSTM based amalgamation for Alzheimer's Disease detection. J Med Biol Eng. 2020;40(5):688-706.
2. Si X, Zhang X, Zhou Y, Sun Y, Jin W, Yin S, et al. Automated detection of juvenile myoclonic epilepsy using CNN based transfer learning in diffusion MRI. IEEE; 2020. p.1679-82.
3. Lee SM, Hyeon JW, Kim S-J, Kim H, Noh R, Kim S, et al. Sensitivity and specificity evaluation of multiple neurodegenerative proteins for Creutzfeldt-Jakob disease diagnosis using a deep-learning approach. Prion. 2019;13(1):141-50.
4. Yang Y, Yan LF, Zhang X, Han Y, Nan HY, Hu YC, et al. Glioma grading on conventional MR images: a deep learning study with transfer learning. Front Neurosci. 2018;12:804.
5. Wang S., Zhan T, Chen Y, Zhang Y, Yang M, Lu H, et al. Multiple sclerosis detection based on biorthogonal wavelet transform, RBF kernel principal component analysis, and logistic regression. IEEE Access, 2016. 4: p.7567-7576.
6. Nayak DR, Dash R, Majhi B. Brain MR image classification using two-dimensional discrete wavelet transform and AdaBoost with random forests. Neurocomputing (Amsterdam). 2016;177:188-97.
7. Zhang Y-D, Pan C, Sun J, Tang C. Multiple sclerosis identification by convolutional neural network with dropout and parametric ReLU. J Comput Sci. 2018;28:1-10.
8. Eitel F, Soehler E, Bellmann-Strobl J, Brandt AU, Ruprecht K, Giess RM, et al. Uncovering convolutional neural network decisions for diagnosing multiple sclerosis on conventional MRI using layer-wise relevance propagation. Neuroimage Clin. 2019;24:102003.
9. Alijamaat A, NikravanShalmani A, Bayat P. Multiple sclerosis identification in brain MRI images using wavelet convolutional neural networks. Int J Imaging Syst Technol. 2021;31(2):778-85.
10. Han J, Hou S-M. Multiple sclerosis detection via wavelet entropy and feedforward neural network trained by adaptive genetic algorithm. Lect Notes Comput Sci. 2019;11507:87-97.
11. Han J, Hou S-M. A multiple sclerosis recognition via hu moment invariant and artificial neural network trained by particle swarm optimization. Lect Notes Inst Comput Sci Soc-Inform Telecommun Eng. 2020;327:254-64.
12. Tang, C. Multiple sclerosis detection via 5-layer convolutional neural network. J Med Imaging Health Inform. 2021. 11: p. 1-8.
13. MRI lesion segmentation in multiple sclerosis database.
14. Alparslan E, Fuatince M. Image enhancement by local histogram stretching. IEEE Trans Syst Man Cybern B Cybern. 1981;11:376-85.
15. Pasban S, Mohamadzadeh S, Zeraatkar-Moghaddam J, Shafiei AK. Infant brain segmentation based on a combination of VGG-16 and U-Net deep neural networks. IET Image Process. 2020;14(17):4756-65.
16. Arulmozhi P, Abirami S. DSHPoolF: deep supervised hashing based on selective pool feature map for image retrieval. Vis Comput. 2021;37(8):2391-405.
17. Krestinskaya O, James AP. Analogue neuro-memristive convolutional dropout nets. Proc Math Phys Eng Sci. 2020;476(2242).
18. Zhang YD, Zhang Z, Zhang X, Wang SH. MIDCAN: A multiple input deep convolutional attention network for Covid-19 diagnosis based on chest CT and chest X-ray. Pattern Recognit Lett. 2021;150:8-16.
19. Clement JC, Indira N, Vijayakumar P, Nandakumar R. Deep learning based modulation classification for 5G and beyond wireless systems. Peer Peer Netw Appl. 2021;14(1):319-32.
20. Wang SH, Satapathy SC, Anderson D, Chen SX, Zhang YD. Deep fractional max pooling neural network for COVID-19 recognition. Front Public Health. 2021;9:726144.
21. Mahmoudi MA, Chetouani A, Boufera F, Tabia H. Learnable

pooling weights for facial expression recognition. Pattern Recognit Lett. 2020;138:644-50.

22. Wu K. SOSPCNN: structurally optimized stochastic pooling convolutional neural network for tetralogy of fallot recognition. Wirel Commun Mob Comput. 2021;2021:5792975.

23. Sahani M, Swain BK, Dash PK. FPGa based favourite skin colour restoration using improved histogram equalization with variable enhancement degree and ensemble extreme learning machine. IET Image Process. 2021;15:1247-59.

24. Lyu C, Hu G, Wang D. Attention to fine-grained information: hierarchical multi-scale network for retinal vessel segmentation. Vis Comput. 2020.

25. Satapathy SC, Wu D. Improving ductal carcinoma in situ classification by convolutional neural network with exponential linear unit and rank-based weighted pooling. Complex Intell Syst. 2021;7:1295-310.

26. Gugushvili S, Mariucci E, der Meulen F. Decompounding discrete distributions: a nonparametric Bayesian approach. Scand J Statist. 2020; 47:464-492.

27. Mukuno J, Matsui. Natural gradient descent of complex-valued neural networks invariant under rotations. IEICE T Fund Electr, 2019. E102A(12): p.1988-1996.

28. Zhang Y-D, Dong Z, Wang S-H, Yu X, Yao X, Zhou Q, et al. Advances in multimodal data fusion in neuroimaging: Overview, challenges, and novel orientation. Inf Fusion. 2020;64:149-87.

29. Wang SH, Zhou Q, Yang M, Zhang YD. ADVIAN: Alzheimer's disease VGG-inspired attention network based on convolutional block attention module and multiple way data augmentation. Front Aging Neurosci. 2021;13:687456.

30. Ryan P, Dilley B, Davies D, Glass T, Abadi F. Short-term movement patterns, population estimates and breeding biology of an island endemic bird, the Tristan Thrush. Revista Brasileira De Ornitologia, 2019. 27(4): p.245-252.

31. Chakraborty S, Khare K. Consistent estimation of the spectrum of trace class Data Augmentation algorithms. Bernoulli. 2019;25(4B):3832-63.

32. Zhang Y, Zhang X, Zhu W. ANC: attention network for COVID-19 explainable diagnosis based on convolutional block attention module. Comput Model Eng Sci. 2021;127(3):1037-58.

33. Shahid AI, Almotairi S. Automated Arabic sign language recognition system based on deep transfer learning. Int J Comput Sci Net Secur. 2019;19(10):144-52.

34. Wang SH, Zhang Y, Cheng X, Zhang X, Zhang YD. PSSPNN: PatchShuffle stochastic pooling neural network for an explainable diagnosis of COVID-19 with multiple-way data augmentation. Comput Math Methods Med. 2021;2021:6633755.

35. Aldabbas H, Asad M, Ryalat MH, Malik KR, Qureshi MZA. Data augmentation to stabilize image caption generation models in deep learning. Int J Adv Comput Sci Appl. 2019;10(10):571-9.

36. Nguyen KD, Nguyen K, Le DD, Duong DA, Nguyen TV. YADA: you always dream again for better object detection. Multimed Tools Appl. 2019;78(19):28189-208.

37. Zhang Y-D, Satapathy SC, Guttery DS, Górriz JM, Wang S-H. Improved breast cancer classification through combining graph convolutional network and convolutional neural network. Inf Process Manag. 2021;58(2):102439.

38. Pho K, Mohammed Amin MK, Yoshitaka A. Segmentation-driven hierarchical retinaNet for detecting protozoa in micrograph. Int J Semant Comput. 2019;13(03):393-413.

39. Wang SH, Nayak DR, Guttery DS, Zhang X, Zhang YD. COVID-19 classification by CCSHNet with deep fusion using transfer learning and discriminant correlation analysis. Inf Fusion. 2021;68:131-148.

40. Arvanitakis K, Avlonitis M, Papadimitriou E. Introducing stochastic recurrence interval to classification algorithms for identifying asperity patterns. Phys A: Stat Mech Appl. 2018;512:566-77.

41. Baquirin RBM, Fernandez PL. Artificial neural network (ANN) in a small dataset to determine neutrality in the pronunciation of English as a foreign language in Filipino Call Center Agents. Inteligencia Artificial-Iberoamerica Journal of Artificial Intelligence. 2018;21(62):134-44.

Alcoholic brain injury via 8-layer deep convolutional neural network

Ziquan ZHU[1,*], Mackenzie BROWN[2,*]

1 Department of Civil Engineering, University of Florida, Gainesville, United States
2 School of Engineering, Edith Cowan University, Joondalup WA 6027, Australia

*Correspondence: Zhu.ziquan@ufl.edu, mackbrown@ieee.org
https://doi.org/10.37175/stemedicine.v2i8.97

ABSTRACT

Alcohol can act quickly in the human body and alter mood and behavior. If people drink too much alcohol, it will accumulate in the liver and brain. To a certain extent, the symptoms of alcoholism will appear. So far, the main method of diagnosis of alcoholic brain injury is through MRI images by radiologists. However, this is a very subjective diagnosis. Radiologists could be influenced by external factors, resulting in diagnostic errors, such as physical discomfort, inattention, lack of rest, etc.. In the paper, we introduced a 8-layer deep convolutional neural network structure for alcoholic brain injury detection. Three fully connected layers, five pooling layers, and five convolution layers formed the proposed neural network structure. We proposed three improvements in this paper, (i) An automatic diagnosis method of alcoholic brain injury based on deep learning was proposed; (ii) We introduced Dropout to the proposed structure to improve robustness; (iii) Compared with other seven advanced approaches, the proposed 8-layer deep convolutional neural network structure is more efficient. The experimental results demonstrated that the specificity, sensitivity, accuracy, precision, FMI MCC and F1 were 96.20 ± 1.47, 96.14 ± 1.99, 96.17 ± 1.55, 95.98 ± 1.54, 96.06 ± 1.62 93.34 ± 3.11, 96.05 ± 1.62, respectively. Based on the comparison results, our method had the excellent performance. The proposed method can be used as one of the methods to detect alcoholic brain injury based on MRI images.

Keywords: Alcoholism · Deep convolution neural network · Dropout · MRI

Introduction

Alcohol, which is present in different proportions in various kinds of alcohol, can act quickly in the human body and alter mood and behavior. It can spread and distribute directly into the bloodstream throughout the body. The liver is where alcohol is mainly metabolized in the body. After entering the human body, a small amount of alcohol can be immediately discharged through the lungs or sweat glands. In the liver, the vast majority of alcohol reacts with alcohol dehydrogenase to produce acetaldehyde. People cannot metabolize alcohol indefinitely. If people drink too much alcohol, it

would accumulate in the liver and brain. When alcohol accumulates in the human body to a certain extent, it will lead to alcoholism. In medicine, alcoholism is medically divided into chronic and acute alcoholism. Acute alcoholism is the central nervous system dysfunction caused by heavy consumption of alcohol or alcoholic beverages over a period of time, which is usually manifested as abnormal behavior and consciousness. Severe damage to organ function can result in respiratory and circulatory failure, and then endanger life. Chronic alcoholism is a serious poisoning of the central nervous system caused by excessive drinking over a long period of time. The human body will not absorb and digest ethanol in alcohol. The ethanol in alcohol flows into the brain through the circulation of blood, further damages the nerve cells in the human brain, causes harm to the central nervous system, leads to the increase of inhibitory neurons, inhibit active neurons, and makes people slow to

respond. Once the excessive accumulation of ethanol in alcohol will cause irreparable damage to nerve cells. Patients with chronic alcoholism encephalopathy may have Wernicke's encephalopathy, Kosakoff syndrome, chronic alcoholic dementia, alcoholic delirium, alcoholic epilepsy, alcoholic psychotropic behavior disorder, and so on. Excessive drinking can also cause an alcoholic coma. Alcoholism is very common in some countries (e.g., Europe, America). Alcoholism is the third leading public health issue in the United States, after cardiovascular disease and cancer.

With the continuous research and development of deep learning, deep learning technology has been widely used in many fields, such as medicine. Lu proposed a radial-basis-function neural network (RBFNN) to detect pathological brains (1). S Sudha used convolutional neural network (CNN) for automatic segmentation of RoI in medical imaging modalities such as carotid artery ultrasound images (2). Y.-C. Hsieh used VGG16 to find out breast MC clusters from the image. Moreover, they used Mask RCNN to find MCs from the clusters to remove the noise from the background (3). S. Kido developed an image-based computer-aided detection (CADe) algorithm by use of regions with CNN features (R-CNN) for detection of lung abnormalities (4). K. Karthik used benchmark deep learning models to improve the quality of diagnostic images, through Super-resolution, for enabling faster and easier detection of anomalies that may be missed otherwise (5). Y, Bar explored the ability of CNN learned from a non-medical dataset to identify different types of pathologies in chest x-rays (6). The best performance was achieved using CNN and GIST features. C.-Y. Sun proposed a novel deformable cascade faster region-based convolutional neural networks (Faster R-CNN) to realize vascular plaque recognition in OCT images (7). W. S. Kim presented a new automatic CAC voxel classification model with multi-scale CNN architecture which can reflect the advantages of large receptive CNN and small receptive CNN (8). W. Li et al. demonstrated a new region-based convolutional neural network framework for multi-task prediction using an epithelial network head and a grading network head (9). Compared with a single-task model, their multi-task model can provide complementary contextual information, which contributes to better performance. L. Li, J introduced a new convolutional neural network structure for medical image denoising-deep neural network based on wavelet domain (deep wavelet denoising net, DWDN) (10).

In the field of AI applied to alcoholism, we have collected results from existing publications. Hou used Hu moment invariant (HMI) to identify alcoholism (11). Yang combined HMI with machine learning (ML) to identify pathological brains (12). Their method is used as a comparison basis in this study. Han proposed a Three-Segment Encoded Jaya (TSEJ) to identify alcoholism (13). Chen, et al. employed fractional Fourier transform (FrFT) to identify pathological brains (14). Their method is used as a comparison method. Qian used cat swarm optimization (CSO) to identify alcoholism (15).

Macdonald employed logistic regression (LR) to identify alcoholism (16). Chen used wavelet energy entropy (WEE) to identify alcoholism (17). Xie presented an AlexNet transfer learning model to identifyalco holism (18).

So far, the main method of diagnosis of alcoholic brain injury is through MRI images by radiologists. However, this is a very subjective diagnosis. Radiologists could be influenced by external factors, resulting in diagnostic errors, such as physical discomfort, inattention, lack of rest, etc.. This paper proposed 8-layer customized deep convolution neural network to address this issue. There arethree improvements in this paper, (i) An automatic diagnosis method of alcoholic brain injury based on deep learning was proposed; (ii) We introduced Dropout to the proposed structure to improve stability and robustness; (iii) Compared with other seven advanced approaches, the proposed 8-layer deep convolutional neural network structure is more efficient.

The structure of paper is as follows: Section 2 introduces the materials, Section 3 talks about the basics of deep convolution neural network (DCNN), Section 4 describes the experimental and comparison results, conclusion in included in Section 5.

Dataset
Subjects

We strictly checked and excluded the data of the research subjects. Participants were first interviewed by computer diagnosis. We would exclude participants with serious mental illness. We would exclude participants who are not in a coma for more than 15 minutes caused by schizophrenia, depression, and alcoholism. If participants suffered from stroke, epilepsy, AIDS and Wernicke-Korsak of syndrome, we excluded them. Finally, the first language of the participants was mandarin, which was also one of requirements.

Participants can participate in the experiment through Nanjing Brain Hospital and Jiangsu Provincial People's Hospital or by Internet advertisements and flyer. We spent three years collecting data from 235 research subjects. All the data in this paper were agreed by the hospitals and participants. There were 121 non-alcoholic control participants in the study, including 59 males and 62 females. In addition, we collected 114 chronic alcohol participants (males-58, females-56) who had long-term abstinence.

Scan

The scanning instrument in this paper was Siemens VERIO TIM 3.0T Magnetic Resonance Scanner. During the scan, 235 participants kept calm and laid down with their eyes closed. MP-RAGE sequence was used to get a total of 216 transection slices of the participants' brain. The imaging parameters were TI = 900 ms, gray level depth = 8-bit, TR = 2000 ms, TE = 2.50 ms, FA = 9 °, FOV = 256 mm × 256 mm, matrix = 256 × 256. It is important to note here that in this paper our images replaced 16-bit
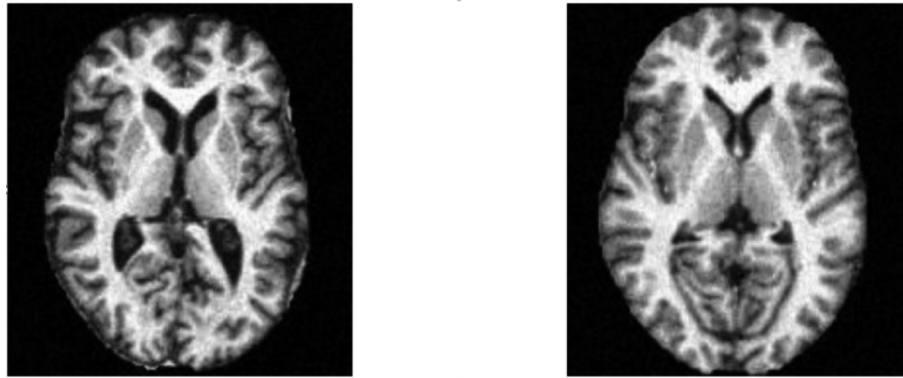
Figure 1. Slice example.

grayscale depth with 8-bit grayscale depth. Alcohol doesn't affect the depth of the brain images, so 8-bit grayscale depth was used in this paper. At the same time, the 8-bit grayscale depth of the images are enough to complete the experiment.

Slice Selection

FMRIB Software Library (FSL) V5.0 software was used to remove the skull and extract the brain. Standard MINI templates were standard for all volumetric images. Then each image is redefined as a 2 mm isotropic voxel. Finally, we selected the slice at G = 80 mm at MNI 152 coordinates, which was obtained linearly by 152-weighted MRI scanning plane, as shown in **Figure 1**. This location was chosen because it is the optimal location of the lateral ventricle and basal ganglia region. Finally we used a matrix of size 176 × 176 for subsequent classification.

Methodology

For the automatic diagnosis of alcoholic brain injury, we used a new method based on deep convolutional neural network (DCNN). Since 2012, deep convolutional neural network has been presented. More and more deep convolution neural network structures with better performance have been designed such as Alexnet (19), ResNet (20), Unet (21), VGGnet (22), and DenseNet (23). Due to the great progress of DCNN, DCNN has been applied in many fields, such as human detection (24), ear

detection (25), etc. DCNN makes the network model no longer complex through three methods: local receptive field, weight sharing, and downsampling. Meanwhile, the depth convolution network structure has no effect on translation, rotation and scaling. In general, the common DCNN is composed of input layer, convolution layers, fully connected layers and output layer, as shown in **Figure 2**.

Figure 2 is a simple DCNN model, which contains three convolution layers, three pooling layers and three pooling layers. Finally, the results are exported through two fully connected layers.

Convolution layer

Convolution layer is the key parts of deep convolution neural network. Convolution layer uses convolution kernel to extract features (26, 27). Convolution kernel is a matrix (28). Starting from the upper left corner of the input matrix, the convolution kernel corresponds to the input matrix range, and then multiplies and adds to get a value (29). In this order, convolution is performed from left to right. This is the principle of convolution layer (30). The convolution layer formula is as follows:

$$W_{o+1} = \frac{W_o - K_w + 2B}{L} + 1 \tag{1}$$

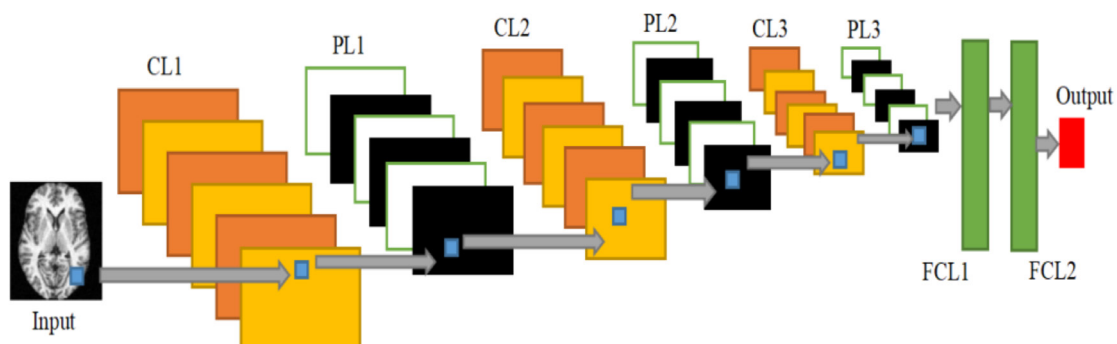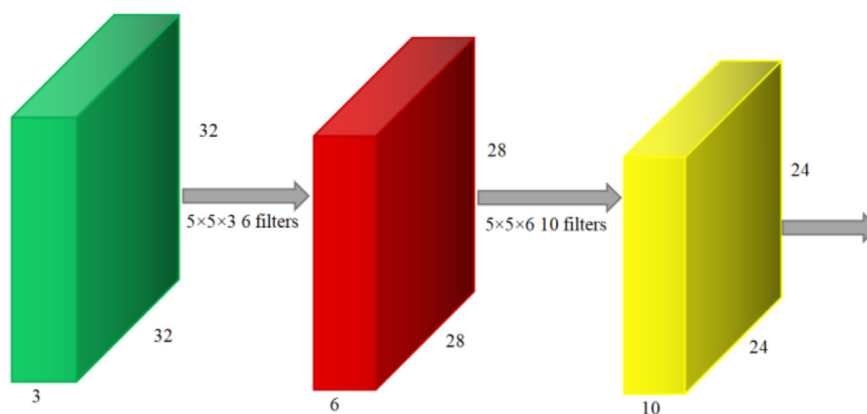$$H_{o+1} = \frac{H_o - K_h + 2B}{L} + 1 \tag{2}$$

Figure 2. DCNN mo.

Figure 3. Convolution operation.

$$Do + 1 = N \tag{3}$$

In the above formula, width is represented by W, height is represented by H, and depth is represented by D, the matrix of input is $W_o \times H_o \times D_o$, the matrix of output is $W_{o+1} \times H_{o+1} \times D_{o+1}$, K_w is the kernel width, K_h represents the kernel height, B is padding, L is stride, N is the kernel width, K_h represents the kernel height, B is padding, L is stride, N is the filters numbers.

Figure 3 is an example of image convolution. The input matrix is $32 \times 32 \times 3$, and 3 is its depth. The first convolution layer is composed of 6 filters with $5 \times 5 \times 3$. After the first convolution, the output matrix is $28 \times 28 \times 6$. The second convolution layer is composed of 10 filters with $5 \times 5 \times 6$. After the second convolution, the output matrix is $24 \times 24 \times 10$.

Figure 4 shows the flow chart of convolution layer.

Pooling layer

The feature map is obtained through convolution layer, and then these features are synthesized and classified. Theoretically, the features extracted from the convolution layer can be used as the input of the classifier. However, too many input values will cause a lot of calculation (31). At this time, the pooling layer is used to reduce the dimension of the feature map (32). There are two advantages for pooling layers: (i) it can make the feature graph smaller, simplify the calculation complexity of the network, reduce the parameters and calculations, and prevent over fitting (33); (ii) the receptive field can be increased by compressing features, extracting features and retaining main features, and keeping scale invariance.

Two methods are usually used for pooling layer, one is maximum pooling and another one is average pooling. Max pooling calculates the maximum value of the location and its adjacent matrix area and takes this maximum value as the value of the location (34). Generally, the average value of adjacent areas is calculated, and the calculated value is taken as the output value. This method is called average pooling. The pooling layer will not have any effect on depth of data matrix, but it can reduce the width and height to accomplish the goal of dimensionality reduction. Specific formula of pooling layer as follows:

$$MaxP = Max(E_C) \tag{4}$$

$$AverP = \frac{\sum E_C}{|E_C|} \tag{5}$$

As the formula above shows, E is the pooling region, C represents the activation set in the pooling region, E_C is elements numbers in the activation set.

Figure 5 shows the different results of different pooling methods. Taking the top left region as an example, the pooling stride of the two pooling methods is 2. The calculation process is as follows: AP = (1+3+5+8)/4 = 4.25; MP = max(1, 3, 5, 8) = 8.

Batch Normalization

For shallow models, data standardization preprocessing will be effective. However, With the continuous training of the model, the parameters of each layer are constantly changing. The closer to the output layer, the less stable the parameters would remain. When we train the deep neural network, although we have standardized the input data before training, the continuous updating of the model will lead to the instability of the output layer (35). Because of the instability of numerical, it is not easy to train a good deep neural network structure with great depth. Batch normalization (BN) continuously adjusts the neural network through the mean and standard deviation of small batches (36). Through this method, the value of each layer of the whole neural network can not fluctuate too much. The structure of batch normalization is shown as **Figure 6**.

Suppose u is the input, W is the weight and b is the deviation parameter. The output is x:

$$x = Wu + b \tag{6}$$

Small batch B composed of m samples, B = {x(1), x(2). . . . x(n)}. Calculate the mean and variance of small batch B:

$$\mu_B \leftarrow \frac{1}{n} \sum_{i=1}^{n} x_i \tag{7}$$

$$\sigma_B^2 \leftarrow \frac{1}{n} \sum_{i=1}^{n} (x_i - \mu_B)^2 \tag{8}$$

The standardization for x_i:

$$\overline{x}_i \leftarrow \frac{x_i - \mu_B}{\sqrt{\sigma_B^2 + \Delta}} \tag{9}$$

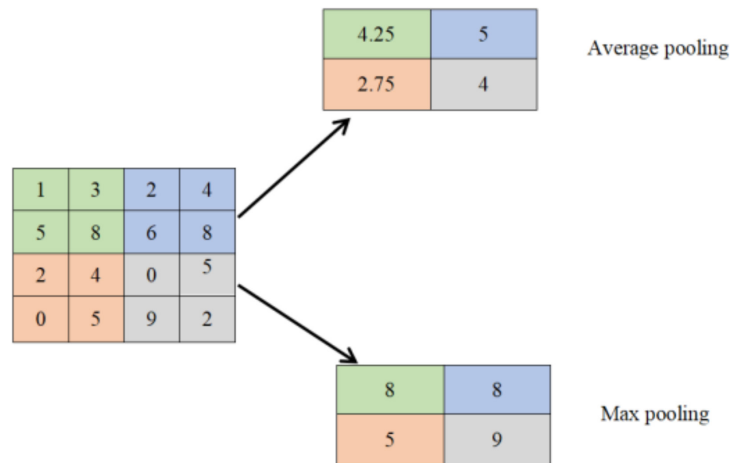**Figure 5. A example of average and max pooling.**

This Δ > 0 is which Δ is a very small number to ensure that the denominator is greater than 0, which makes the formula and the results meaningful. Introduce learnable parameter: scale parameter φ And shift parameters ω.

$$y_i \leftarrow \varphi \overline{x}_i + \omega \qquad (10)$$

Dropout

In the deep learning structure, if the parameters of the structure are too many and the training samples are too few, over fitting is a common problem in trained models (37). The phenomenon of over fitting could appear in neural network training, which is shown in the following aspects (38): the structure has small loss function and high prediction accuracy in the training data. However, contrary to the results obtained from the training data, the model has large loss function and low prediction accuracy. If the model is over fitted, the resulting model can hardly be used (39). Dropout can be one of the solutions to reduce over fitting. In each training, by neglecting half of the feature detectors. It can significantly alleviate the problem of over fitting. The interaction between feature detectors (hidden layer nodes) can be reduced through dropout. **Figure 7** shows the difference between using dropout and not using dropout in deep learning.

Rectified Linear Unit

In the neuron, after the input is summed by weighting, the activation function is applied, as shown in **Figure 8**. The operation of the activation function is to activate some neurons in the neural network and transmit the activation information to the next layer of neural network (40). In order to increase neural network model nonlinearity, activation function is added. When there is no activation function, the output value of each layer in the convolutional neural network structure is a linear function (41). The output is the linear function of the input, which is the most primitive perceptron (42). In order to make the deep convolution neural network closer to the nonlinear function, a nonlinear factor is introduced into the activation function. In this way, deep neural network is suitable for a lot of nonlinear models (43). The activation function can also construct a sparse matrix to eliminate the redundancy in the data and retain the characteristics of the data as much as possible. The most commonly used activation functions are sigmoid and relu function, as shown in **Figure 9**. The formula of relu and sigmoid function:

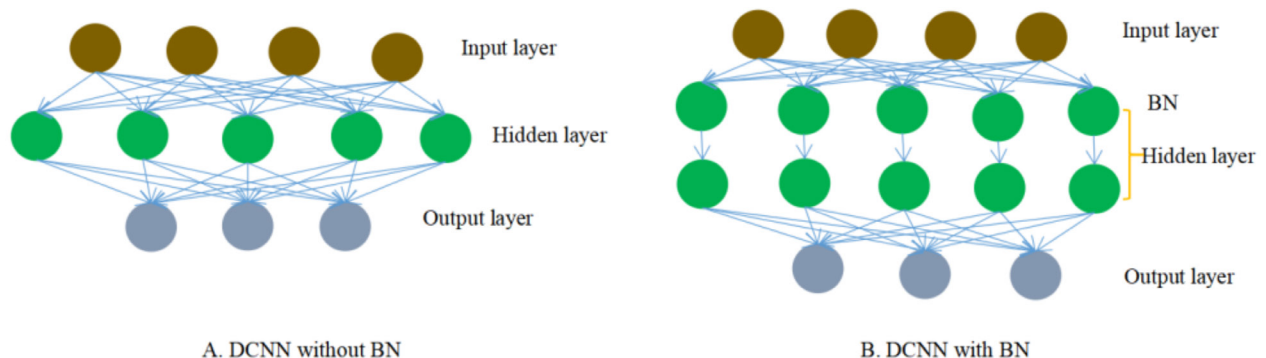$$relu = \begin{cases} 0, & \text{if } x \leq 0 \\ x, & \text{if } x > 0 \end{cases} \qquad (11)$$
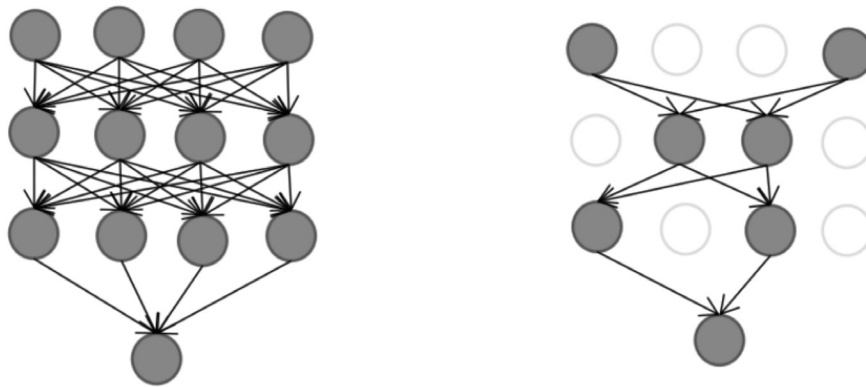

Figure 6. Structure of BN.

Figure 7. An example of network with dropout.

Comparing relu and sigmoid functions, (i) the sigmoid function has a problem of gradient vanishing. In contrast, the output of relu function is very stable, because it is a linear function when x > 0, and the problem of gradient disappearance is avoided; (ii) the calculation of sigmoid function is large; using relu function can save a large number of computation; (iii) the output of some neurons of relu function could be zero, which reduces the relationship between parameters and the density of the network, thus reducing the possibility of over fitting. Based on the above advantages, we used the relu function in this paper.

Structure of customized DCNN

In the paper, we introduced a 8-layer deep convolutional neural network structure for alcoholic brain injury detection. Three fully connected layers, five pooling layers, and five convolution layers formed the proposed neural network structure. Each convolution layer is connected to the pooling layer, and dropout is in front of each fully connected layer. The structure of 8-layer DCNN is shown in **Figure 10**.

The parameter settings of 8-layer DCNN structure are shown in **Table 1**. The input size is 176×176. The filter size of each convolution layer is 3×3. The number of filters in the first convolution layer is 32, that in the second convolution layer is 64, that in the third convolution layer is 128, that in the forth convolution layer is 256, and that in the fifth convolution layer is 512. After five times convolution and pooling, three dropout and three fully connected layers are added, and the final output size is 2.

Measures

For the evaluation index of binary classification, the results are divided into positive and negative categories. In the actual classification, there are four categories. Suppose the confusion matrix is:

$$\text{confusion matrix} = \begin{bmatrix} TP & FN \\ FP & TN \end{bmatrix} \qquad (13)$$

TP represents True Positive; FN is False Positive; FN represents False Negative; TN is True Negative. In the paper, seven indicators are used to evaluate the model.

$$\text{Sensitivity} = \frac{TP}{TP + FN} \qquad (14)$$

$$\text{Specificity} = \frac{TN}{FP + TN} \qquad (15)$$

$$\text{Precision} = \frac{TP}{TP + FP} \qquad (16)$$

$$\text{Accuracy} = \frac{TP + TN}{TP + FP + TN + FN} \qquad (17)$$
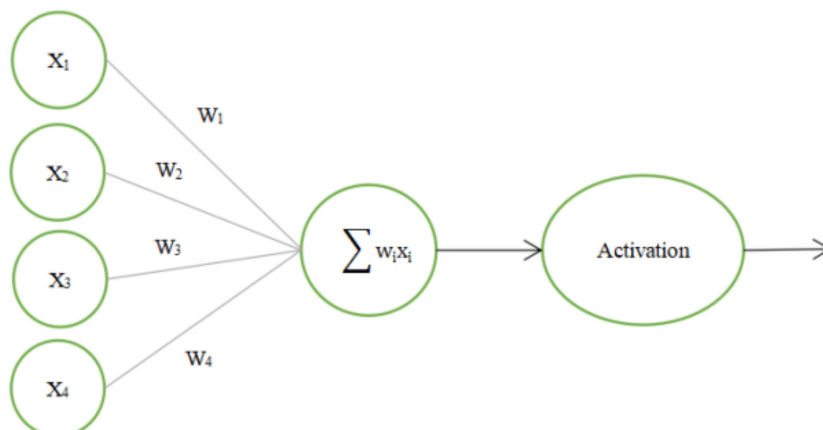
$$F1 = \frac{2TP}{2TP + FP + FN} \qquad (18)$$

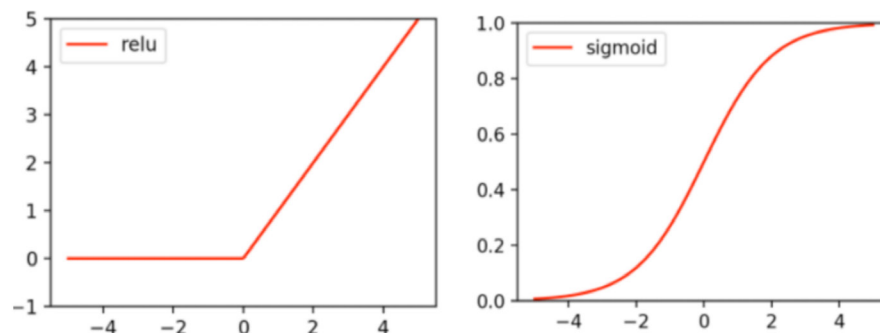**Figure 8. Schematic diagram of activation function.**

Figure 9. relu and sigmoid function.

$$MCC = \frac{TP \times TN - TP \times FN}{\sqrt{(TP + FP) \times (TP + FN) \times (TN + FP) \times (TN + FN)}} \qquad (19)$$

$$FMI = \frac{TP}{\sqrt{(TP + FP) \times (TP + FN)}} \qquad (20)$$

In order to avoid contingency, 10 runs were carried out, and the mean and variance of each indicators were calculated.

Experiment Result
Statistical Analysis
In this paper, we ran 10 times and got ten groups of data. Each time the division was updated randomly. The experimental results are shown in **Table 2**. The average of specificity, sensitivity, accuracy, precision, FMI MCC and F1 were 96.20 ± 1.47, 96.14 ± 1.99, 96.17 ± 1.55, 95.98 ± 1.54, 96.06 ± 1.62 93.34 ± 3.11, 96.05 ± 1.62, respectively. From **Figure 11**, we can get this conclusion that the eighth group is the best and the sixth group is the eighth group is the best and the sixth group is the worst.

Comparison with State-of-the-art Approaches
We compare the proposed "8-layer customized DCNN" with seven advanced approaches: HMI (11), HMI+ML (12), TSEJ (13), FrFT (14), CSO (15), LR (16), WEE (17). We have described these advanced approaches in detail in the first chapter introduction. Table 3 shows the comparison test results. The accuracy of the proposed DCNN structure is 96.17 ± 1.55. Our accuracy is at least 2% higher than that of other seven approaches. HMI (11) yields 89.15, HMI + ML (12) obtains 85.15, TSEJ (13) gets 93.66, FrFT [14] achieves 86.77, CSO (15) obtains 92.13, LR (16) gets 83.70 ± 1.35, WEE (17) achieves 92.55 ± 0.67. It is easy to conclude that the DCNN structure which is introduced in the paper has superior performance than these seven approaches. For clear view, a comparison plot is shown in **Figure 12**.

Conclusion
In the paper, we introduced a 8-layer deep convolutional neural network structure for alcoholic brain injury detection. Three fully connected layers, five pooling layers, and five convolution layers formed the proposed neural network structure. In this framework, we added dropout to reduce over fitting problem. We compared our

Table 1. Parameter settings of deep convolutional neural network.

Layers	Size	Parameters
Input	176 × 176	
Conv Layer -first	88 × 88 × 32	32 3 × 3, pooling size = 2
Conv Layer -second	44 × 44 × 64	64 3 × 3, pooling size = 2
Conv Layer -third	22 × 22 × 128	128 3 × 3, pooling size = 2
Conv Layer -forth	11 × 11 × 256	256 3 × 3, pooling size = 2
Conv Layer -fifth	5 × 5 × 512	512 3 × 3, pooling size = 2
Dropout-1		0.5
FCL-1	1000	12800 × 1000
Dropout-2		0.5
FCL-2	100	1000 × 100
Dropout-3		0.5
FCL-3	2	100 × 2
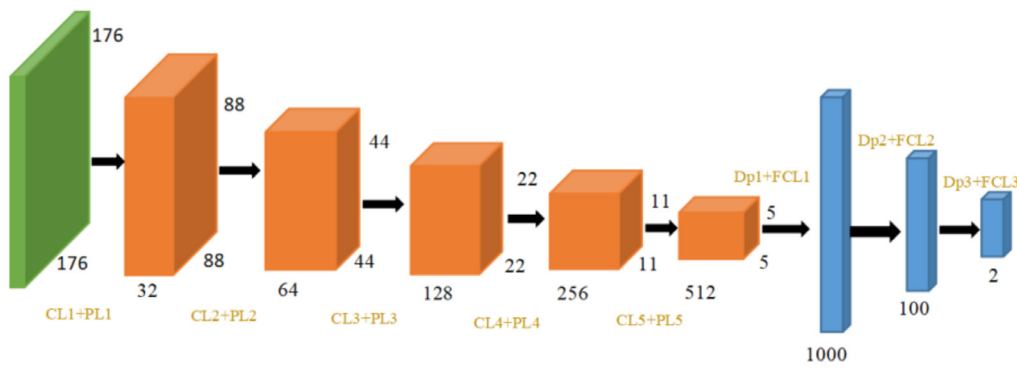
Figure 10. Structure of DCNN.

Table 2. Experimental result.

| Run	sensitivity	specificity	precision	accuracy	F1	MCC	FMI
1	97.37	97.52	97.37	97.45	97.37	94.89	97.37
2	96.49	96.69	96.49	96.60	96.49	93.19	96.49
3	98.25	97.52	97.39	97.87	97.82	95.75	97.82
4	96.49	95.04	94.83	95.74	95.65	91.50	95.66
5	94.74	96.69	96.43	95.74	95.58	91.49	95.58
6	92.11	94.21	93.75	93.19	92.92	86.38	92.92
7	93.86	95.04	94.69	94.47	94.27	88.93	94.27
8	98.25	98.35	98.25	98.30	98.25	96.59	98.25
9	97.37	94.21	94.07	95.74	95.69	91.54	95.70
10	96.49	96.69	96.49	96.60	96.49	93.19	96.49
MSD	96.14 ± 1.99	96.20 ± 1.47	95.98 ± 1.54	95.98 ± 1.54	96.05 ± 1.62	92.34 ± 3.11	96.06 ± 1.62
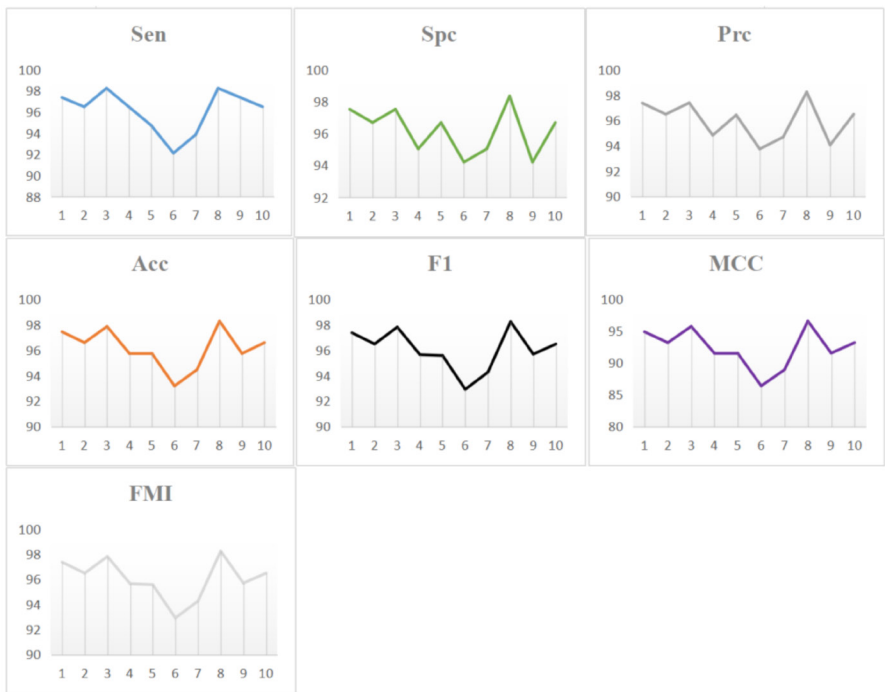
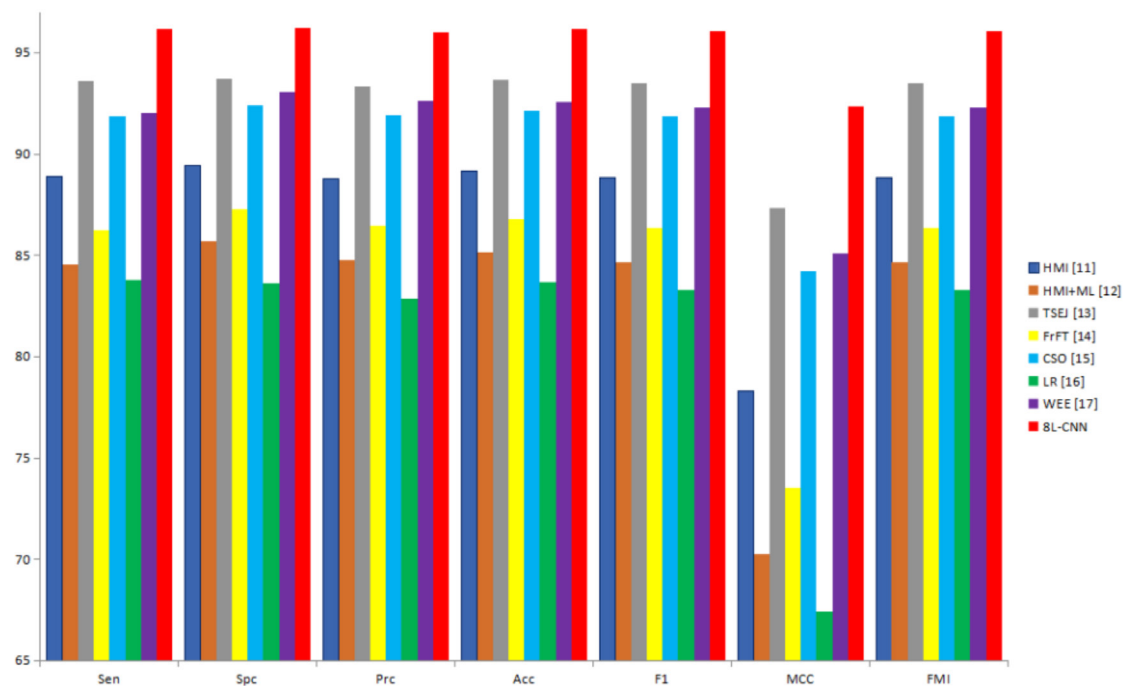**Table 2. Experimental result.**

Figure 12. comparison of seven state-of-the-art approache.

method with other seven advanced approaches to test the performance of the DCNN structure. According to the comparison test results, we validated the DCNN structure had the excellent performance. The proposed model can be used as one of the methods to detect alcoholic brain injury based on MRI images.

The limitations of the paper: (i) there are very few training data set. With the number of cases increases and the amount of training increases, the performance of the system will achieve higher accuracy; (ii) we did not compare DCNN structures with different number of hidden layers.

In the next paper, more data will be collected in our next experiment to test performance. Meanwhile, getting the best combination of hidden layers is also one of the main purposes of our next paper. What's more, some new technologies may be applied to our next paper for comparison, such as transfer learning pre-trained models.

Conflict of interest
The authors declare that they have no conflicts of interest to disclose.

References
1. Lu Z, Lu S, Liu G, Zhang Y, Yang J, Phillips P. A pathological brain detection system based on radial basis function neural network. J Med Imaging Health Inform. 2016;6:1218-1222.
2. Sudha S, Jayanthi KB, Rajasekaran C, Sunder T, editors. Segmentation of RoI in medical images using CNN- a comparative study. TENCON 2019 - 2019 IEEE Region 10 Conference (TENCON); 2019 17-20 Oct. 2019.
3. Hsieh YC, Chin CL, Wei CS, Chen IM, Yeh PY, Tseng RJ, editors. Combining VGG16, Mask R-CNN and Inception V3 to identify the benign and malignant of breast microcalcification clusters. 2020 International Conference on Fuzzy Theory and Its Applications (iFUZZY); 2020 4-7 Nov. 2020.
4. Kido S, Hirano Y, Hashimoto N, editors. Detection and classification of lung abnormalities by use of convolutional neural network (CNN) and regions with CNN features (R-CNN). 2018 International Workshop on Advanced Image Technology (IWAIT); 2018 7-9 Jan. 2018.

Table 3. The comparison results.

Method	Sen	Spc	Prc	Acc	F1	MCC	FMI
HMI [11]	88.86	89.42	88.78	89.15	88.82	78.28	88.82
HMI+ML [12]	84.56	85.70	84.78	85.15	84.67	70.27	84.67
TSEJ [13]	93.60	93.72	93.35	93.66	93.47	87.31	93.47
FrFT [14]	86.23	87.27	86.46	86.77	86.34	73.51	86.34
CSO [15]	91.84	92.40	91.92	92.13	91.88	84.24	91.88
LR [16]	83.77 ± 2.42	83.64 ± 2.33	82.88 ± 1.90	83.70 ± 1.35	83.29 ± 1.42	67.44 ± 2.66	83.31 ± 1.41
WEE [17]	92.02 ± 1.13	93.06 ± 1.42	92.61 ± 1.36	92.55 ± 0.67	92.30 ± 0.67	85.11 ± 1.35	92.31 ± 0.68
8L-CNN (Ours)	96.14 ± 1.99	96.20 ± 1.47	95.98 ± 1.54	96.17 ± 1.55	96.05 ± 1.62	92.34 ± 3.11	96.06 ± 1.62

5. Karthik K, Kamath SS, Kamath SU, editors. Automatic quality enhancement of medical diagnostic scans with deep neural image super-resolution models. 2020 IEEE 15th International Conference on Industrial and Information Systems (ICIIS); 2020 26-28 Nov. 2020.

6. Bar Y, Diamant I, Wolf L, Lieberman S, Konen E, Greenspan H, editors. Chest pathology detection using deep learning with non-medical training. 2015 IEEE 12th International Symposium on Biomedical Imaging (ISBI); 2015 16-19 April 2015.

7. Sun CY, Hong XJ, Shi S, Shen ZY, Zhang HD, Zhou LX. Cascade Faster R-CNN Detection for Vulnerable Plaques in OCT Images. IEEE Access. 2021;9:24697-704.

8. Kim WS, Jung HY, Choi JH, editors. Automatic CAC voxel classification with multi-scale CNN architecture. 2019 International Conference on Information and Communication Technology Convergence (ICTC); 2019 16-18 Oct. 2019.

9. Li W, Li J, Sarma KV, Ho KC, Shen S, Knudsen BS, et al. Path R-CNN for prostate cancer diagnosis and gleason grading of histological images. IEEE Trans Med Imaging. 2019;38(4):945-54.

10. Li L, Wu J, Jin X. CNN denoising for medical image based on wavelet domain. in 2018 9th International Conference on Information Technology in Medicine and Education (ITME), Hangzhou, China, 2018;pp 105-109.

11. Zhang Y-D, Zhang Y, Lv Y-D, Hou X-X, Liu F-Y, Jia W-J, et al. Alcoholism detection by medical robots based on Hu moment invariants and predator–prey adaptive-inertia chaotic particle swarm optimization. Comput Electr Eng. 2017;63:126-138.

12. Zhang Y, Yang J, Wang S, Dong Z, Phillips P. Pathological brain detection in MRI scanning via Hu moment invariants and machine learning. J Exp Theor Artif Intell. 2016;29:299-312.

13. Wang S-H, Muhammad K, Lv Y, Sui Y, Han L, Zhang Y-D. Identification of alcoholism based on wavelet Renyi entropy and three-segment encoded Jaya algorithm. Complexity. 2018;2018:3198184.

14. Zhang Y-D, Chen S, Wang S-H, Yang J-F, Phillips P. Magnetic resonance brain image classification based on weighted-type fractional Fourier transform and nonparallel support vector machine. Int J Imaging Syst Technol. 2015;25;317-327.

15. Zhang Y-D, Sui Y, Sun J, Zhao G, Qian P. Cat Swarm Optimization applied to alcohol use disorder identification. Multimed Tools Appl. 2018;77:22875-22896.

16. Yuanyuan T, Felix M, editors. Alcoholism Detection via Wavelet Energy and Logistic Regression. Proceedings of the 2018 International Conference on Information Technology and Management Engineering (ICITME 2018); 2018 2018/08: Atlantis Press.

17. Chen X and Yan Y. Alcoholism detection by wavelet energy entropy and linear regression classifier. Cmes-comp Model Eng. 2021;127:325--343.

18. Wang S-H, Xie S, Chen X, Guttery DS, Tang C, Sun J, et al. Alcoholism identification based on an AlexNet transfer learning model. Front Psychiatry. 2019;10:205.

19. Krizhevsky A, Sutskever I, Hinton GE. ImageNet classification with deep convolutional neural networks. Commun ACM. 2017;60:84-90.

20. He K, Zhang X, Ren S, Sun J. Deep residual learning for image recognition. in 2016 IEEE Conference on Computer Vision and Pattern Recognition (CVPR), Las Vegas, NV, USA, 2016 pp. 770-778.

21. Ronneberger O, Fischer P, Brox T, editors. U-Net: Convolutional networks for biomedical image segmentation. Medical Image Computing and Computer-Assisted Intervention – MICCAI 2015; 2015 2015//; Cham: Springer International Publishing.

22. Long J, Shelhamer E, Darrell T. Fully convolutional networks for semantic segmentation. in 2015 IEEE Conference on Computer Vision and Pattern Recognition (CVPR), Boston, MA, USA, 2015 pp. 3431-3440.

23. Huang G, Liu Z, Van Der Maaten L, Weinberger KQ. Densely connected convolutional networks. in 2017 IEEE Conference on Computer Vision and Pattern Recognition (CVPR), Honolulu, HI, USA, 2017 pp. 2261-2269.

24. Kim JH, Hong HG, Park KR. Convolutional neural network-based human detection in nighttime images using visible light camera sensors. Sensors (Basel). 2017;17(5):1065.

25. Cintas C, Quinto-Sánchez M, Acuña V, Paschetta C, de Azevedo S, Cesar Silva de Cerqueira C, et al. Automatic ear detection and feature extraction using Geometric Morphometrics and convolutional neural networks. IET Biometrics. 2017;6:211-223.

26. Hwang C, Kim D, Lee T. Semi-supervised based unknown attack detection in EDR environment. KSII Trans Internet Inf Syst. 2020;14:4909-4926.

27. Jung H and Lee BG. The impact of transforming unstructured data into structured data on a churn prediction model for loan customers. KSII Trans Internet Inf Syst. 2020;14:4706-4724.

28. Wang S-H, Wu K, Chu T, Fernandes SL, Zhou Q, Zhang Y-D, et al. SOSPCNN: structurally optimized stochastic pooling convolutional neural network for tetralogy of fallot recognition. Wirel Commun Mob Comput. 2021;2021:5792975.

29. Altwaijry N. Keystroke dynamics analysis for user authentication using a deep learning approach. Int J Comput Sci Inf Secur. 2020;20:209-216.

30. Zhang Y-D, Satapathy SC, Wu D, Guttery DS, Górriz JM, Wang S-H. Improving ductal carcinoma in situ classification by convolutional neural network with exponential linear unit and rank-based weighted pooling. Complex Intell Syst. 2021;7:1295-1310.

31. Afrasiabi S, Afrasiabi M, Mohammadi M, Parang B. Fault localisation and diagnosis in transmission networks based on robust deep Gabor convolutional neural network and PMU measurements. IET Gener Transm Distrib. 2020;14:6484-6492.

32. Wang S-H, Zhou Q, Yang M, Zhang Y-D. ADVIAN: alzheimer's disease VGG-inspired attention network based on convolutional block attention module and multiple way data augmentation. Front Aging Neurosci. 2021;13:687456.

33. Sahani M, Swain B, Dash P. FPGA-based favourite skin colour restoration using improved histogram equalization with variable enhancement degree and ensemble extreme learning machine. IET Image Process. 2021;15:1247-1259.

34. Zhang Y, Zhang X, Zhu W. ANC: attention network for COVID-19 explainable diagnosis based on convolutional block attention module. Comput Model Eng Sci. 2021;127:1037-1058.

35. Suzuki H, Yoshitaka T, Yoshio TA-O, Tada T. Artificial intelligence for cancer detection of the upper gastrointestinal tract. Dig Endosc. 2021;33:254-262.

36. Wang S-H, Zhang Y, Cheng X, Zhang X, Zhang Y-D. PSSPNN: PatchShuffle stochastic pooling neural network for an explainable diagnosis of COVID-19 with multiple-way data augmentation. Comput Math Methods Med. 2021;2021:6633755.

37. Trasolini R, Byrne MF. Artificial intelligence and deep learning for small bowel capsule endoscopy. Dig Endosc. 2021;33:290-297.

38. Hirasawa T, Ikenoyama Y, Ishioka M, Namikawa K, Horiuchi Y, Nakashima H, et al. Current status and future perspective of artificial intelligence applications in endoscopic diagnosis and management of gastric cancer. Dig Endosc. 2021;33:263-272.

39. Zhang Y-D, Satapathy SC, Guttery DS, Górriz JM, Wang S-H. Improved breast cancer classification through combining graph convolutional network and convolutional neural network. Inf Process Manag. 2021;58:102439.

40. Corazza PA-O, Maddison J, Bonetti P, Guo L, Luong V, Garfinkel A, et al. Predicting wet age-related macular degeneration (AMD) using DARC (detecting apoptosing

retinal cells) AI (artificial intelligence) technology. Expert Rev Mol Diagn. 2021;21:109-118.

41. Zhang YD, Satapathy SC, Liu S, Li GR. A five-layer deep convolutional neural network with stochastic pooling for chest CT-based COVID-19 diagnosis. Mach Vis Appl. 2021;32:14.

42. Joshi S, Kumar R, Dwivedi A. Hybrid DSSCS and convolutional neural network for peripheral blood cell recognition system. IET Image Process. 2020;14:4450-4460.

43. Wang S-H, Govindaraj VV, Górriz JM, Zhang X, Zhang Y-D. Covid-19 classification by FGCNet with deep feature fusion from graph convolutional network and convolutional neural network. Inf Fusion. 2021;67:208-229.

MicroRNA-155 inhibitor ameliorates collagen-induced arthritis by modulating the phenotype of pro-inflammatory macrophages in a mouse model

Yuanliang CHEN[1][#], Hong Sung MIN[2][#], Yongbai WAN[1], Chaolai JIANG[2], Xiaowei YU[1, 2][*]

1 Department of Orthopaedic Surgery, Haikou Orthopedic and Diabetes Hospital of Shanghai Sixth People's Hospital, Hainan 570311, China.
2 Department of Orthopaedic Surgery, Shanghai Jiao Tong University Affiliated Sixth People's Hospital, Shanghai 200233, China.
# these authors contributed equally to this work.

*Correspondence: yuxw@sjtu.edu.cn
https://doi.org/10.37175/stemedicine.v2i8.105

ABSTRACT

Background: Here, we aimed to illustrate the roles of microRNA (miR)-155 in collagen-induced arthritis (CIA) and its underlying mechanisms.

Methods: A mouse model of CIA was first established, and miR-155 inhibitor was intravenously injected. In *in vitro* studies, bone marrow-derived macrophages (BMDMs) were induced to M1 macrophages followed by the treatment of miR-155 inhibitor. RT-qPCR was applied to determine the mRNA expression. The frequency of M1 or M2 macrophages was determined by flow cytometry. Western blotting was employed to detect protein expression. Enzyme-linked immunosorbent assay was employed to measure the production of inflammatory cytokines and anti-collagen antibody.

Results: The levels of miR-155 were increased in macrophages from rheumatoid arthritis (RA) patients and M1 macrophages. The treatment of miR-155 inhibitor decreased inflammatory cytokines in M1 macrophages. Besides, treatment of miR-155 inhibitors promoted the differentiation of M0 macrophages into M2 macrophages. *In vivo* studies showed that miR-155 inhibitors ameliorated the RA symptoms by decreasing inflammatory cytokines in the CIA mouse model. Treatment of miR-155 also led to decreased M1 macrophage biomarker and increased M2 macrophage biomarker.

Conclusion: MiR-155 inhibitor ameliorates RA symptoms in part by regulating macrophage phenotypes.

Keywords: MicroRNA-155 · Arthritis · Collagen-induced arthritis · Macrophages · Macrophage polarization

Introduction

RA (rheumatoid arthritis), as an autoimmune disease, is characterized by synovial inflammation and the destruction of bones and cartilages (1, 2). The development of RA also induces other tissue damages including the vascular system, lung, heart, and skins (1). The prevalence and incidence of RA are 1% and 0.03%, respectively, worldwide (3). Besides, the medical cost for RA is more than 5,000 dollars per patient per year (3). Although it is reported to be associated with inflammation, the underlying mechanisms of RA is still unclear.

Many studies have demonstrated that macrophages are involved in RA pathology by the production of pro-inflammatory cytokines, such as tumor necrosis factor (TNF)-α, interleukin (IL)-6 and IL-1 (4, 5). The activation of inflammation-related signaling pathways also triggers the release of adhesion molecules, which recruits the leukocytes to the damaged tissues (4). Typical macrophages in activated condition are M1 or M2 types (6), also called classical and alternative activated macrophage, respectively (7). Previous studies have demonstrated that M1 macrophages could produce vast

inflammatory cytokines, thus accelerate the process of RA, while M2 macrophages could attenuate inflammation and repair the tissues (6, 8). Importantly, M1 macrophages can be shifted into M2 phenotype (7).

MicroRNAs (miRNAs, miRs) have been identified to play crucial roles in the modulation of gene expression (9). Interestingly, macrophage polarization can also be regulated by miRNAs (10). Previous studies have demonstrated that miR-9, miR-127, miR-155, and miR-125b promote M1 polarization, whereas miR-124, miR-223, miR-132, and miR-146a induce M2 polarization (11). Therefore, the regulation of miRNAs is a good strategy for the regulation of macrophage polarization. In 2011, Stephan and colleagues found that miR-155 knockout mice could not develop collagen-induced arthritis (CIA), indicating that miR-155 contributes to the pathogenesis development of CIA (12). Furthermore, Su and colleagues reported that the levels of miR-155 were increased in RA animal models and patients. The knockdown of miR-155 ameliorates the development of RA. All these results demonstrated the important roles of miR-155 in RA (13).

Materials and Methods
Patients and healthy volunteers

All participants signed the documents of consent. The study was approved by Haikou Orthopedic and Diabetes Hospital of Shanghai Sixth People's Hospital. Peripheral blood was collected from RA patients and healthy volunteers. The peripheral blood mononuclear cells (PBMCs) were isolated based on the published protocol (14). Macrophages were then separated from PBMCs for further assays.

Animals

Animal studies were approved by Haikou Orthopedic and Diabetes Hospital of Shanghai Sixth People's Hospital. Male DBA/1 mice were housed under humidity (60 ± 5%) and temperature-controlled (22-24 °C) condition. A CIA mouse model was established by immunizations of bovine type 2 collagen that was emulsified in complete or incomplete Freund's adjuvant at day 0 and day 21.

The mice were divided into phosphate-buffered saline (PBS) group, control inhibitor group, and miR-155 inhibitor group. In the PBS group, the mice were intravenously injected with PBS on day 15 and day 31. In the control inhibitor group and miR-155 inhibitor group, the mice were intravenously injected with control inhibitors or miR-155 inhibitors (50 μg per mouse) that were mixed with Entranster-in vivo at day 15 and day 31.

In the experimental period, the CIA score and ankle thickness were measured every two days. An X-ray was applied to determine the joint damage induced by arthritis at the end of the experiment. After the mice were sacrificed, the joint tissues, blood were collected.

Histopathology examination

The mice were sacrificed at the end of the experiments.

The joint tissues were collected, then fixed in formalin solution (10%) prior to embedding in paraffin. Hematoxylin and eosin staining was conducted. A microscope was used for the observation of the slides.

Bone marrow-derived macrophage (BMDM) isolation and culture

BMDMs were isolated based on the published protocol (15). Briefly, the collected cells were maintained in DMEM (Dulbecco's modified eagle medium) with M-CSF (macrophage colony-stimulating factor, 10 ng/ml) and 10% fetal bovine serum for 5 days. To generate M1 macrophages, cells were incubated with interferon (IFN)-γ (50 ng/mL) and lipopolysaccharides (LPS) (100 ng/mL) for 24 h. After phenotype examination, M1 macrophages were treated with miR-155 inhibitor or control inhibitor.

Enzyme-linked immunosorbent assay (ELISA)

Inflammatory cytokine levels including IL-6, MCP-1 (monocyte chemoattractant protein 1), IL-1β, TNF-α, and anti-collagen antibody were determined using ELISA based on the manufacturers' documents.

Flow cytometry analysis

After the polarized macrophages were transfected with miR-155 inhibitor or control inhibitor, cell suspension was prepared and stained with PE-Cy7 conjugated MHCII and PE-conjugated CD206. FlowJ (BD FACSCalibur) was applied to analyze the results.

RT-qPCR

RNA was isolated using RNA extraction kit. The melt curves were used to analyze the accuracy. Gene expression was calculated using $2^{-\Delta\Delta Ct}$ values with GAPDH as control.

Western blotting

The protein was extracted following routine procedures (16, 17). Briefly, the joint tissue was lysed using cold radioimmunoprecipitation assay buffer with protease inhibitor. Then, the extraction buffer was centrifuged (13,000 g) for 15 mins to remove insoluble materials and sample debris. Concentrations of extracted proteins were quantified using BCA protein assay kits. The protein was then loaded, subjected to separation using sodium dodecyl sulfate polyacrylamide gel electrophoresis. The gels were transferred to polyvinylidene fluoride membranes, which were blocked with 5% non-fat milk at room temperature for 2 hours. Primary antibodies against inducible nitric oxide synthase (iNOS) or CD206 were used for incubation with the membranes at 4 °C overnight. Appropriate secondary antibodies conjugated with horseradish peroxidase were used.

Statistics

Data were shown as mean ± standard deviation (SD). One-way analysis of variance with Student-Newman-Keuls test and multiple comparisons were employed for the data comparison. Statistical significance was
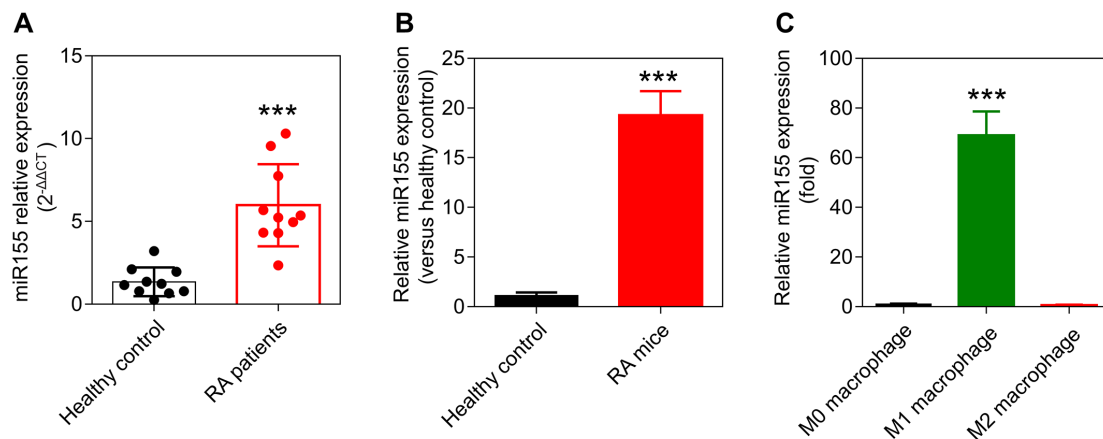
Figure 1. (A) qRT-PCR was determined to detect the mRNA levels of miR-155 in the macrophages that were isolated from PBMCs in the RA patients and healthy control (n = 10). (B) The mRNA levels of miR-155 in the macrophages isolated from collagen-induced arthritis (CIA) mouse model (n = 8). (C) The mRNA levels of miR-155 in M0, M1 and M2 macrophages. Data were shown as mean ± SD, ***$p < 0.001$.

determined when p value was less than 0.05.

Results

MiR-155 was upregulated in macrophages of RA patients and M1 macrophages

We first investigated the mRNA levels of miR-155 in healthy volunteers and RA patients. mRNA levels of miR-155 in the macrophages from PBMCs of RA patients were remarkably enhanced when compared to the healthy volunteers ($p < 0.001$, **Figure 1A**). Next, we analyzed the mRNA levels of miR-155 in the macrophages from RA mouse model and healthy mice. Interestingly, the mRNA levels of miR-155 in the macrophages of RA mice were significantly increased when compared to the healthy control mice ($p < 0.001$, **Figure 1B**). Finally, to investigate the relationship of miR-155 expression pattern and macrophage phenotype, we determined the mRNA levels of miR-155 in M0 macrophages and polarized M1 and M2 macrophages. mRNA levels of miR-155 were much higher in M1 macrophages in comparison to M0 and M2 macrophages ($p < 0.001$, **Figure 1C**), suggesting that miR-155 expression pattern is associated with the inflammatory status of macrophages.

MiR-155 inhibitor decreased the production of inflammatory cytokines in M1 macrophages

The effects of miR-155 inhibitor on the production of inflammatory cytokines in M1 macrophages were further examined. To obtain M1 macrophages, BMDMs were stimulated with IFN-γ (50 ng/mL) and LPS (100 ng/mL). We observed the levels of inflammatory cytokines including TNF-α, IL-1β, IL-6, and MCP-1 were obviously decreased in M1 macrophages in the presence of miR-155 inhibitors in a concentration-dependent manner (**Figure 2A-D**).

Effects of MiR-155 inhibitors on the inflammatory gene expression and macrophages phenotype

We then explored the potential of miR-155 on the expressions of inflammatory genes. To obtain M1 macrophages, BMDMs were stimulated with IFN-γ (50 ng/mL) and LPS (100 ng/mL) followed by the treatment of miR-155 inhibitors (**Figure 3A**). Interestingly, we observed that, in the presence of miR-155 inhibitors, the gene expressions of M1 macrophage-related biomarkers including IL-12 and Nos2 was significantly decreased, whereas the gene expression of M2 macrophage-related biomarkers including Arg1 and Mrc1 was significantly increased (**Figure 3B**). We inferred that miR-155 might affect macrophages polarization. Besides, we also analyze the population of M1 and M2 macrophages. miR-155 inhibitors significantly reduced the percentage of MHC IIhi macrophages ($p < 0.001$, **Figure 3C** and **D**) and increased the percentage of CD206hi macrophages ($p < 0.001$, **Figure 3E** and **F**).

Effects of miR-155 inhibitors on the RA symptoms of CIA mouse model

To confirm the effects of miR-155 inhibition in vitro, the effects of miR-155 in a CIA mouse model were investigated. As shown in **Figure 4A**, a CIA mouse model was established by immunizations of bovine type 2 collagen emulsified in complete or incomplete Freund's adjuvant. The mice were intravenously injected with control inhibitors or miR-155 inhibitors (50 μg per mouse) that were mixed with Entranster-in vivo at day 15 and day 31. We observed that the miR-155 inhibitors significantly decreased the RA score and mean ankle diameter at day 34 in comparison to the control inhibitor group (**Figure 4B and C**). At the end of the experimental period, X-ray was applied to determine the joint change in each group. We observed that arthritic changes in the PBS and control inhibitor group, whereas the treatment of miR-155 inhibitor ameliorated these changes (**Figure 4D**).
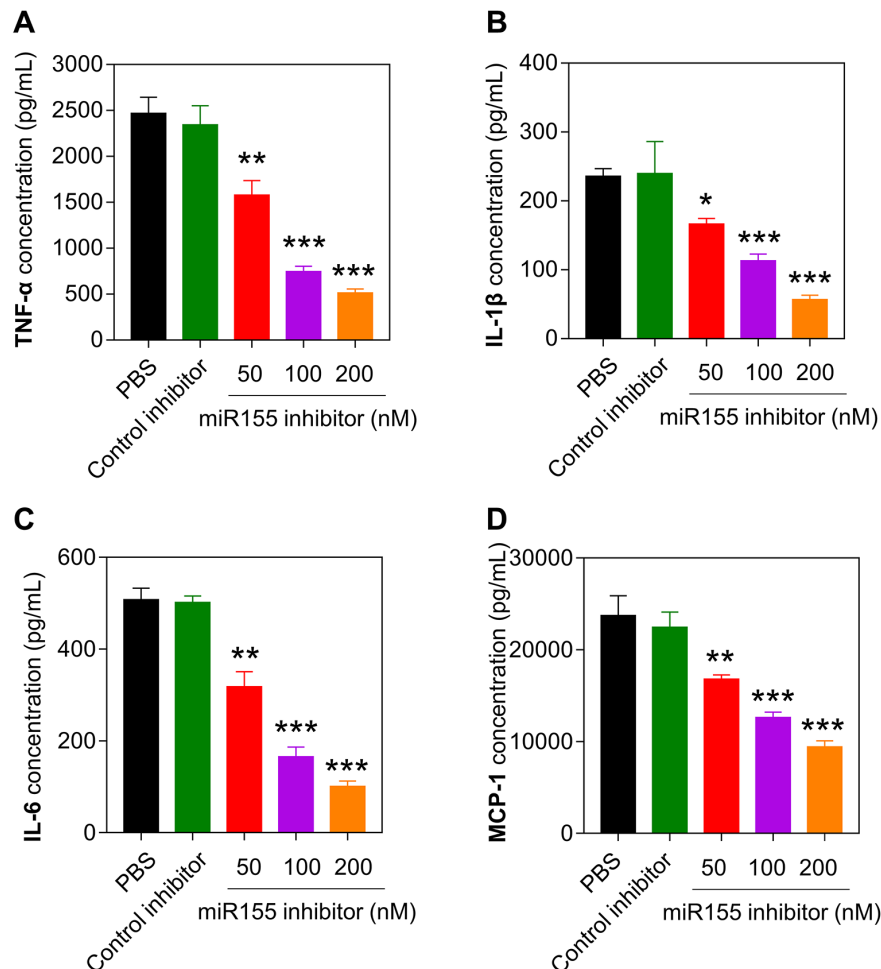
Figure 2 Inflammatory cytokines including TNF-α (A), IL-1β (B), IL-6 (C), and MCP-1 (D) in M1 macrophages transfected with miR-155 inhibitors were determined using ELISA. To induce M1 macrophages, BMDMs were incubated with LPS (100 ng/mL) and IFN-γ (50 ng/mL) for 24 and then transfected with miR-155 inhibitors for another 48 h. Data were shown as means ± SD, *$p < 0.05$, **$p < 0.01$, and ***$p < 0.001$ vs M1 macrophage transfected with control inhibitor.

Treatment of miR-155 inhibitor attenuated CIA symptoms

Finally, the effects of miR-155 inhibitor on the CIA symptoms were evaluated. Histopathological examination demonstrated synovial lining and bone erosions and proliferation of synovial membrane cells in the PBS and control inhibitor groups, whereas synovial lining and bone erosions were ameliorated and fewer numbers of synovial membrane cells were observed in the miR-155 inhibitor groups (**Figure 5A**). These results demonstrated that the treatment of miR-155 inhibitor reversed the histopathological changes in RA. Additionally, miR-155 inhibitor decreased the levels of anti-collagen IgG in comparison to the PBS and control inhibitor groups (**Figure 5B**).

The expressions of M1/ M2 macrophages biomarkers and inflammatory cytokines were studied. The results demonstrated that miR-155 inhibitor-treated resulted in a decrease of M1 macrophage biomarker iNOS and an increase of M2 macrophage biomarker CD206, suggesting that the levels of miR-155 are associated with the changes of macrophage phenotypes (**Figure 5C**). Furthermore, the

results also showed the levels of inflammatory cytokines including TNF-α, IL-1β, and IL-6 were significantly decreased in the presence of miR-155 inhibitor, indicating the inhibition of miR-155 attenuated the expressions of inflammatory cytokines in the joint tissue of CIA mouse (**Figure 5D-F**).

Discussion

In the present study, the mRNA level of miR-155 was found to be increased in CIA animal models and RA patients. Notably, our results showed a significant increase of miR-155 in M1 macrophages as compared to M0 and M2 macrophages. We further analyzed the relationship between miR-155 and macrophage polarization.

First, we found that miR-155 inhibitor decreased inflammatory cytokines in M1 macrophages. Second, miR-155 inhibitor promoted the polarization of macrophages into M2 phenotypes. The in vivo studies also confirmed the regulatory effects of miR-155 inhibitor on the macrophage phenotype and RA symptoms. Therefore, we speculated that the inhibition of miR-155 might be a
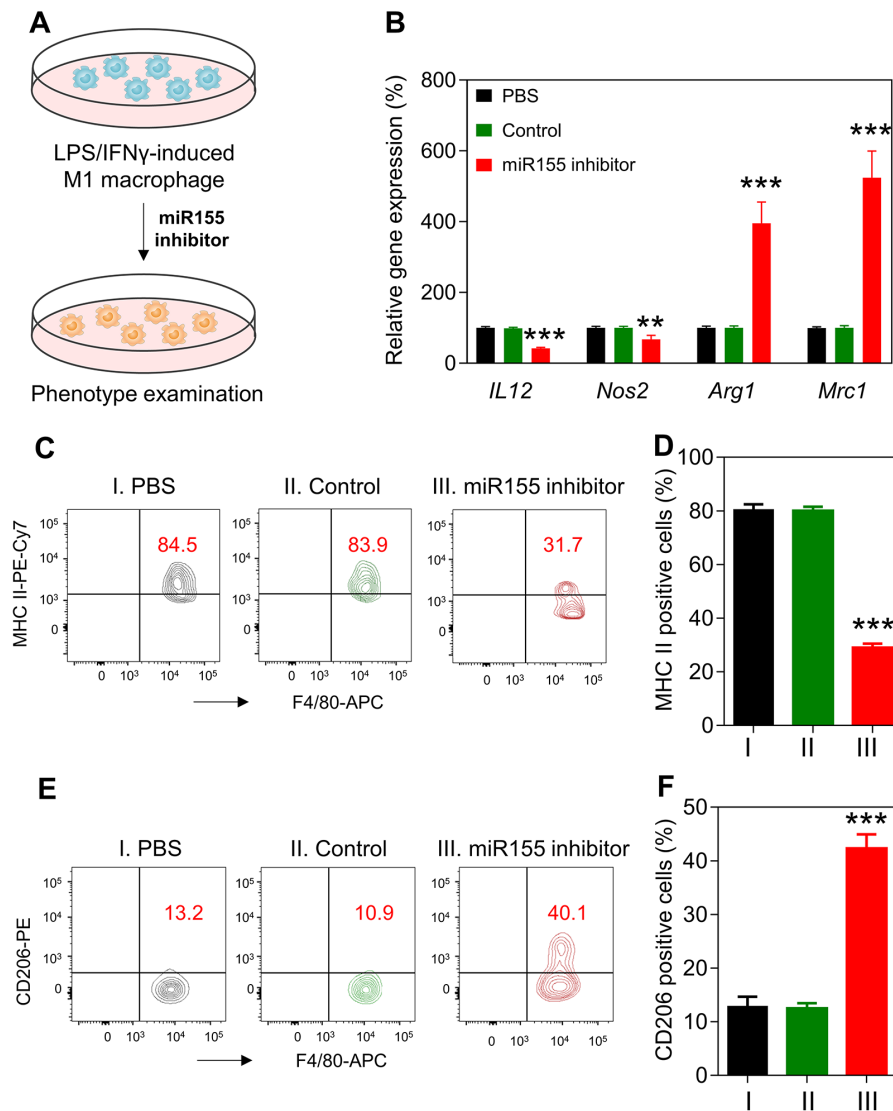
Figure 3 (A) Diagram of the generation of M1 macrophages. BMDMs were incubated with LPS plus IFN-γ and the phenotype was determined after transfection of miR-155 inhibitor for 48 h. (B) qRT-PCR was determined to detect the mRNA levels of IL12, Nos2, Arg1, and Mrc1 in M1 macrophages after the treatment of miR-155 inhibitor. (C-F) Flow cytometry was applied to determine the percentage of MHCII positive macrophages and CD206 positive macrophages after treatment. Data were shown as means ± SD, **$p < 0.01$, ***$p < 0.001$ (vs M1 macrophage treated with control inhibitor).

promising strategy for RA treatment.

The role of macrophages in RA occurrence and development has been well documented (5, 8, 18). The inflammatory mediators and cytokines secreted by macrophages trigger an adaptive immune response in the synovium and contributes to the local joint destruction (4, 19, 20). Here, we specifically determined the expressions of miR-155 in the macrophages. miR-155 was significantly increased in the macrophages from PBMCs of RA patients and in the BMDMs. Our findings are consistent with previous studies, in which an elevation of miR-155 is observed in RA animal models and patients.

Furthermore, activated macrophages in joint tissue are including M1 or M2 phenotypes (7). M1 is called classical activated macrophage whereas M2 is recognized as an alternative activated macrophage (8). M1 phenotypes accelerate the process of RA by the release of large

amounts of inflammatory mediators such as iNOS and other pro-inflammatory cytokines, whereas M2 phenotypes could exert anti-inflammatory activities via the secretion of anti-inflammatory cytokines (21, 22). In this study, the expressions of miR-155 in the different types of macrophages including M0, M1, and M2 were all determined. The results showed that the mRNA levels of miR-155 were much higher in M1 macrophages as compared to the other two phenotypes. We then explored the relationship between miR-155 and inflammatory cytokines in the M1 macrophages. Interestingly, we found that the inflammatory cytokines including IL-6, IL-1β, TNF-α and chemokine MCP-1 were significantly decreased in the presence of miR-155 inhibitors. These results demonstrated that inhibition of miR-155 reduced the expressions of inflammatory cytokines and chemokines.
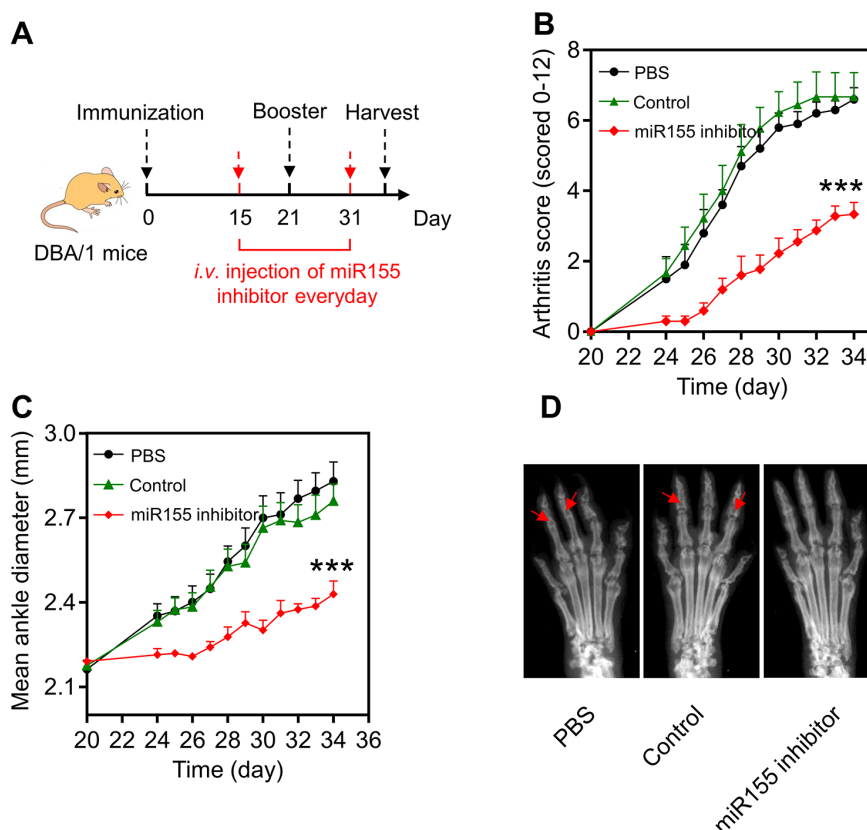
Figure 4 (A) The schematic diagram showed the process of immunization and treatment methods on the CIA mouse model. To establish a CIA model, the mice were immunized twice with bovine type 2 collagen emulsified in Freund's adjuvant. Next, the mice were intravenously injected with 50 µg miR-155 inhibitor or control inhibitor on 15th and 31th day. In the experimental period, CIA score (B) and ankle thickness (C) were determined every two days. At the end of the experimental period, (D) X-ray was applied to evaluate the joint damage. Data were shown as means ± SD, ***$p < 0.001$ (vs mice injected with control inhibitor).

It has been verified that M1 macrophages can be shifted into M2 phenotypes (23). M1 to M2 transition ameliorates the inflammatory status, leading to the resolution of inflammation and tissue repair in RA (7). We next sought the effects of miR-155 inhibitor on the regulation of macrophages polarization. It is known that M1 macrophages produce iNOS and pro-inflammatory cytokine IL-12, while genes including Arg1 and Mrc1 were highly expressed in the M2 macrophages (24, 25). Our results demonstrated that M1 macrophage-related biomarkers were significantly decreased whereas M2 macrophage-related biomarkers were significantly increased in the presence of miR-155 inhibitor. In addition to detection of the M1 or M2 macrophages related genes, we also explored the effects of miR-155 inhibitor on the frequency of M1 and M2 macrophages. M1 macrophages can be characterized by MHC-IIhi while M2 macrophages can be characterized by CD206hi (26, 27). Interestingly, our results suggested that miR-155 inhibitors promoted the polarization of M2 macrophages.

CIA mouse model was established to determine the effects of miR-155 inhibitor on the RA symptoms, inflammatory cytokine expressions, and macrophages phenotypes. We observed the increase of mean ankle and RA scores in the experimental period. Besides, we also found that arthritic changes including 1) synovial lining

and bone erosions, 2) proliferation of synovial membrane cells, 3) an increase of anti-collagen IgG in serum, and 4) the increase of inflammatory cytokines in the joint tissue. These results supported that the CIA mouse model was successfully constructed (28, 29). Interestingly, the treatment of miR-155 inhibitor significantly decreased the RA score and mean ankle diameter. At the end of the experimental period, X-ray and histopathology examinations supported that the treatment of miR-155 inhibitor ameliorated the arthritic changes and pathophysiology of RA.

Finally, we determined the effects of miR-155 inhibitor on the macrophage phenotypes and expressions of inflammatory cytokine. Interestingly, the results demonstrated that the treatment of miR-155 inhibitor promoted the polarization of M2 phenotypes and reduced the polarization of M1 phenotypes. The also showed inflammatory cytokines were remarkably decreased in the presence of miR-155 inhibitor, indicating the inhibition of miR-155 also ameliorated the inflammation in the joint tissues.

Conclusion

We observed that miR-155 was increased in RA patients and CIA animal models. Treatment of miR-155 inhibitor
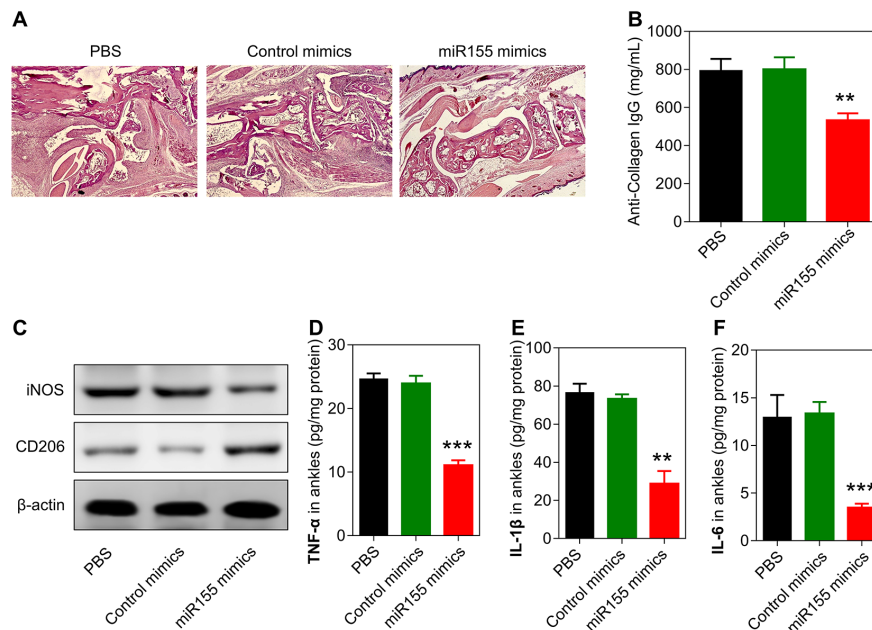
Figure 5. Figure 5 (A) Histopathology examination was performed and represented histopathology pictures showed the ankle joints in each group. (B) ELISA was applied to measure the serum anti-collagen antibody. (C) Western blot was applied to determine the protein expressions of iNOS and CD206 in the ankle joint tissues. (D-F) ELISA was applied to determine the levels of TNF-α, IL-1β, and IL-6 in the joint tissues. Data were shown as mean ± SD, **$p < 0.001$, ***$p < 0.001$ (vs mice injected with control inhibitor).

decreased inflammatory cytokines in M1 macrophages and promoted M2 macrophages polarization. Additionally, miR-155 inhibitor ameliorated the RA pathological changes and decreased inflammatory cytokines and resulted in the changes of macrophage phenotypes. In summary, microRNA-155 inhibitor ameliorates RA symptoms in part by regulating macrophage phenotypes.

Conflict of interest

The authors declare that they have no conflicts of interest to disclose.

References
1. Firestein GS. Evolving concepts of rheumatoid arthritis. Nature. 2003;423(6937):356-61.
2. Decker JL, Malone DG, Haraoui B, Wahl SM, Schrieber L, Klippel JH, et al. NIH conference. Rheumatoid arthritis: evolving concepts of pathogenesis and treatment. Ann Intern Med. 1984;101(6):810-24.
3. Alamanos Y, Drosos AA. Epidemiology of adult rheumatoid arthritis. Autoimmun Rev. 2005;4(3):130-6.
4. Choy EH, Panayi GS. Cytokine pathways and joint inflammation in rheumatoid arthritis. N Engl J Med. 2001;344(12):907-16.
5. Ma Y, Pope RM. The role of macrophages in rheumatoid arthritis. Curr Pharm Des. 2005;11(5):569-80.
6. Wang Y, Han CC, Cui D, Li Y, Ma Y, Wei W. Is macrophage polarization important in rheumatoid arthritis? Int Immunopharmacol. 2017;50:345-52.
7. Tardito S, Martinelli G, Soldano S, Paolino S, Pacini G, Patane M, et al. Macrophage M1/M2 polarization and rheumatoid arthritis: a systematic review. Autoimmun Rev. 2019;18(11):102397.
8. Siouti E, Andreakos E. The many facets of macrophages in rheumatoid arthritis. Biochem Pharmacol. 2019;165:152-69.
9. Liu G, Abraham E. MicroRNAs in immune response and macrophage polarization. Arterioscler Thromb Vasc Biol. 2013;33(2):170-7.
10. Wu XQ, Dai Y, Yang Y, Huang C, Meng XM, Wu BM, et al. Emerging role of microRNAs in regulating macrophage activation and polarization in immune response and inflammation. Immunology. 2016;148(3):237-48.
11. Essandoh K, Li Y, Huo J, Fan GC. MiRNA-mediated macrophage polarization and its potential role in the regulation of inflammatory response. Shock. 2016;46(2):122-31.
12. Bluml S, Bonelli M, Niederreiter B, Puchner A, Mayr G, Hayer S, et al. Essential role of microRNA-155 in the pathogenesis of autoimmune arthritis in mice. Arthritis Rheum. 2011;63(5):1281-8.
13. Su LC, Huang AF, Jia H, Liu Y, Xu WD. Role of microRNA-155 in rheumatoid arthritis. Int J Rheum Dis. 2017;20(11):1631-7.
14. Pauley KM, Satoh M, Chan AL, Bubb MR, Reeves WH, Chan EK. Upregulated miR-146a expression in peripheral blood mononuclear cells from rheumatoid arthritis patients. Arthritis Res Ther. 2008;10(4):R101.
15. Weischenfeldt J, Porse B. Bone marrow-derived macrophages (BMM): isolation and applications. CSH Protoc. 2008:pdb prot5080.
16. Liu C, Zhao J, Liu Y, Huang Y, Shen Y, Wang J, et al. A novel pentacyclic triterpenoid, Ilexgenin A, shows reduction of atherosclerosis in apolipoprotein E deficient mice. Int Immunopharmacol. 2016;40:115-24.
17. Yang H, Wang J, Fan JH, Zhang YQ, Zhao JX, Dai XJ, et al. Ilexgenin A exerts anti-inflammation and anti-angiogenesis effects through inhibition of STAT3 and PI3K pathways and exhibits synergistic effects with Sorafenib on hepatoma growth. Toxicol Appl Pharmacol. 2017;315:90-101.

18. Maruotti N, Cantatore FP, Crivellato E, Vacca A, Ribatti D. Macrophages in rheumatoid arthritis. Histol Histopathol. 2007;22(5):581-6.

19. Ridgley LA, Anderson AE, Pratt AG. What are the dominant cytokines in early rheumatoid arthritis? Curr Opin Rheumatol. 2018;30(2):207-14.

20. Zhang A, Lee YC. Mechanisms for joint pain in rheumatoid arthritis (RA): from cytokines to central sensitization. Curr Osteoporos Rep. 2018;16(5):603-10.

21. Udalova IA, Mantovani A, Feldmann M. Macrophage heterogeneity in the context of rheumatoid arthritis. Nat Rev Rheumatol. 2016;12(8):472-85.

22. Soler Palacios B, Estrada-Capetillo L, Izquierdo E, Criado G, Nieto C, Municio C, et al. Macrophages from the synovium of active rheumatoid arthritis exhibit an activin A-dependent pro-inflammatory profile. J Pathol. 2015;235(3):515-26.

23. Lawrence T, Natoli G. Transcriptional regulation of macrophage polarization: enabling diversity with identity. Nat Rev Immunol. 2011;11(11):750-61.

24. Jablonski KA, Amici SA, Webb LM, Ruiz-Rosado Jde D, Popovich PG, Partida-Sanchez S, et al. Novel markers to delineate murine M1 and M2 macrophages. PLoS One. 2015;10(12):e0145342.

25. Aron-Wisnewsky J, Tordjman J, Poitou C, Darakhshan F, Hugol D, Basdevant A, et al. Human adipose tissue macrophages: m1 and m2 cell surface markers in subcutaneous and omental depots and after weight loss. J Clin Endocrinol Metab. 2009;94(11):4619-23.

26. Weisser SB, McLarren KW, Kuroda E, Sly LM. Generation and characterization of murine alternatively activated macrophages. Methods Mol Biol. 2013;946:225-39.

27. Kaplan M, Shur A, Tendler Y. M1 Macrophages but not M2 macrophages are characterized by upregulation of CRP expression via activation of NFkappaB: a possible role for Ox-LDL in macrophage polarization. Inflammation. 2018;41(4):1477-87.

28. Yang GH, Zhang C, Wang N, Meng Y, Wang YS. Anacardic acid suppresses fibroblast-like synoviocyte proliferation and invasion and ameliorates collagen-induced arthritis in a mouse model. Cytokine. 2018;111:350-6.

29. Wang J, Li Y, Li L, Yang J, Kopecek J. Exploration and evaluation of therapeutic efficacy of drug-free macromolecular therapeutics in collagen-induced rheumatoid arthritis mouse model. Macromol Biosci. 2020:e1900445.

Dual coronary embolization associated with atrial fibrillation: a case report

Yonggang YUAN, Zesheng XU*

Department of cardiology, Cangzhou Central Hospital, No. 16 Xinhua Road, Cangzhou 061000, Hebei, China

*Correspondence: xuzeshengc@sina.com
https://doi.org/10.37175/stemedicine.v2i8.99

ABSTRACT

Background: Thrombotic occlusion of the coronary artery, which succeeds the atherosclerotic plaque rupture or erosion, gives rise to a major portion of acute myocardial infarction (AMI) incidences. Nevertheless, coronary embolism is gaining increasing recognition as another important factor contributing to AMI.

Case presentation: A 72-year-old woman with atrial fibrillation (AF) and diabetes mellitus histories, presented with chest pain radiating to the left arm and shoulder that began 6 hours prior to admission. Electrocardiogram revealed AF plus ST-segment elevation in the anterior leads.

Intervention: Patient was first treated with anti-platelet agents (aspirin plus ticagrelor) and atorvastatin. Emergency coronary angiography depicted multi-site coronary embolization of the left circumflex artery (LCX) and the left anterior descending artery (LAD). Blood flow was not restored after intracoronary injection of 600 ug tirofiban. 40 mg recombinant human prourokinase was then administered via aspiration thrombectomy catheter.

Outcome: Two weeks later, coronary angiography showed no residual obstructive lesion in the LCX and LAD with TIMI (thrombolysis in myocardial infarction) 3 flow.

Conclusion: Primary percutaneous coronary intervention is the most effective measure. In the case of failed blood flow restoration, thrombolytic treatment in both intravenous and intracoronary route should be considered.

Keywords: Embolization · Acute myocardial infarction · Atrial fibrillation · Thrombolytic treatment

Introduction

The characteristics of acute myocardial infarction (AMI) include atherosclerotic plaque rupture, fissure, ulceration, dissection or erosion with subsequent thrombus in coronary arteries in most cases, which leads to a disturbed balance between the demand and supply of myocardial oxygen and subsequent myocardial necrosis (1).

Clinically, myocardial ischemia can often be identified based on the medical history of the patient as well as the electrocardiography. Symptoms of ischemia include upper extremity, chest, epigastric or mandibular pain or discomfort (at rest with exertion), or ischemic equivalents such as dyspnea or fatigue, which may last about 20 min. In most cases, the AMI-associated discomfort is diffuse - not positional, nor localized, and not altered by local movements - and it is sometimes accompanied by nausea, syncope, and diaphoresis. Those symptoms, however, are not myocardial ischemia specific, and therefore may be mistakenly diagnosed as gastrointestinal, pulmonary, musculoskeletal, or neurological disorders. Further, it is

possible that MI occurs with only atypical symptoms (eg. cardiac arrest or palpitations), or no symptom at all; for instance in female patients, diabetics, post-operative or critically ill patients, or the elderly (2). Cautious assessment of such patients is encouraged, particularly with a falling and/or rising trend of cardiac biomarkers.

Meanwhile, coronary artery embolism (CE) is regarded as a significant non-atherosclerotic factor contributing to AMI. However, its prevalence is still not clear due to the difficulty to generate acute diagnosis (3). Atrial fibrillation (AF) is the leading cause of CE, and correlates with high risks of thromboembolic incidence. The AF prevalence is predicted to rise due to population aging (4). However, the clinical characteristics, incidence rate, and prognosis of AF remain largely elusive.

We hereby described a case study of a 72 year old female who was admitted to our hospital with persistent AF and ST elevation myocardial infarction (STEMI).

Case description

This study was performed in June 2020 in Department of cardiology, Cangzhou Central Hospital. A 72-year-old female with histories of complete atrioventricular block, persistent AF, and diabetes mellitus, presented with complaints regarding chest pain radiating to the left arm and shoulder that began 6 hours prior to her arrival. Electrocardiogram revealed AF, complete atrioventricular block and ST-segment elevation in the anterior leads. 10 minutes after first medical contact she was given a combination of antiplatelet agents (aspirin, ticagrelor, IIb/IIIa receptor inhibitors) and atorvastatin. Emergency coronary angiography demonstrated multi-site coronary embolization, with abrupt 'cut-off' at the proximal of the left anterior descending artery (LAD) and the distal end of the left circumflex artery (LCX). No significant obstructive lesion was found in the right coronary artery (**Figure 1**).
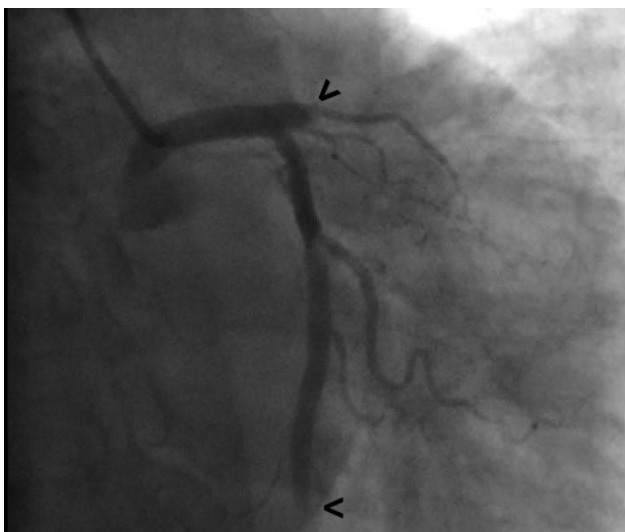

Figure 2. Coronary angiography after 2 weeks showed no residual obstructive lesions in the LAD and the LCX with TIMI 3 flow.

Despite that emergency thrombo-aspiration as well as balloon angioplasty was performed, the coronary blood flow kept TIMI (thrombolysis in myocardial infarction) 0 flow. Still, there appeared no improvement in the blood flow after intracoronary injection of 600 ug tirofiban. In consideration of her past history of untreated AF together with the angiography finding, AF-related coronary artery embolus was highly suggestive as the underlying pathophysiological evidence of the STEMI. 40 mg recombinant human prourokinase was then administered via aspiration thrombectomy catheter.

Two weeks later, she underwent another coronary angiography showed that no residual obstructive lesions in the LAD and the LCX with TIMI 3 flow (**Figure 2**).

Discussion

AMI events are mainly the results of thrombotic occlusion of coronary arteries following rupture or erosion of atherosclerotic plaques. Nevertheless, CE is increasingly acknowledged as a vital non-atherosclerotic factor to induce AMI (3). In a prior report using coronary angiography or autopsy data, 4 ~ 7% of patients with AMI had no atherosclerotic coronary disease (5). Another study based on autopsy findings reported that coronary artery embolic infarct was found in ~13% patients (55 out of 419) (6).

The current report on CE prevalence may be an underestimation, considering that elevated risks of thromboembolic incidence have been observed in patients with rheumatic valvular diseases, prosthesis, cardiomyopathy, intra-cardiac shunts, chronic AF, infective endocarditis, tumors, and several other hypercoagulable states (7, 8). As CE is less often, there is currently a lack of consensus guidelines for CE treatments. Among the possible therapeutic options, triple anti-platelet therapy

Figure 1. Emergency coronary angiography, arrow heads indicate abrupt 'cut-off' sites.

(clopidogrel, IIb/IIIa receptor inhibitors, aspirin) (9), intracoronary catheter aspiration (10), PTCA (11), implantation of stents (12), as well as coronary arterial thrombectomy (13) have been shown to be successful.

However, in our case, despite of thrombus aspiration and balloon dilatation, as well as intracoronary injection of IIB/IIIA antagonist agent, were administered to the patient, there was no restore of blood flow of coronaries.

In the century that angioplasty still under-developed, thrombolytic treatment was the standard treatment for STEMI. However, it gets rarely practiced nowadays following the advance of primary percutaneous coronary intervention (PCI) technique. The most common cause of STEMI resulted from coronaries thrombosis is AF, and the most common origin of thrombus is the left appendage. The thrombus may be well organized. The pathophysiological components are different from the thrombus of unstable plaque rupture. Thrombus aspiration may do well in taking out the thrombus in order to restore blood flow, but not necessarily able to remove all the thrombus.

The standard treatment for cerebral thromboembolic event caused by AF is intravenous thrombolysis, and the successful rate is getting higher as the development of new lytic agent with less complication. Considered as a thromboembolic complication of AF, STEMI resulted by coronaries thromboembolism should receive thrombolytic treatment, and it might give a better outcome. Indeed, our patient was given alteplase lytic treatment after failed PCI, and repeated coronary angiography also showed resolution of clot. In retrospectively reconsideration, the thrombolytic treatment effect might be better if the drug was given via intracoronary route while intervention is ongoing.

Conclusion

In summary, CE-associated STEMI in AF patients is indeed a rare situation. Early systemic anti-thrombosis therapy as well as patient compliance are required to alleviate both short- and long-term adverse effects. Nonetheless, novel approaches for more effective CE treatments in the future are warranted.

Conflict of interest
The authors declare that they have no conflicts of interest to disclose.

References

1. Thygesen K, Alpert JS, Jaffe AS, Simoons ML, Chaitman BR, White HD, et al. Third universal definition of myocardial infarction. Eur Heart J. 2012;33(20):2551-67.
2. Thygesen K, Task Force M, Alpert JS, Task Force M, White HD, Task Force M, et al. Universal definition of myocardial infarctionKristian Thygesen, Joseph S. Alpert and Harvey D. White on behalf of the Joint ESC/ACCF/AHA/WHF Task Force for the Redefinition of Myocardial Infarction. Eur Heart J. 2007;28(20):2525-38.
3. Shibata T, Kawakami S, Noguchi T, Tanaka T, Asaumi Y, Kanaya T, et al. Prevalence, clinical features, and prognosis of acute myocardial infarction attributable to coronary artery embolism. Circulation. 2015;132(4):241-50.
4. Chugh SS, Blackshear JL, Shen W-K, Hammill SC, Gersh BJ. Epidemiology and natural history of atrial fibrillation: clinical implications. J Am Coll Cardiol. 2001;37(2):371-8.
5. Waller BF. Atherosclerotic and nonatherosclerotic coronary artery factors in acute myocardial infarction. Cardiovasc Clin. 1989;20(1):29-104.
6. Prizel K, Hutchins GM, Bulkley BH. Coronary artery embolism and myocardial infarction: A clinicopathologic study of 55 patients. Ann Intern Med. 1978;88(2):155-61.
7. Park HS, Park JH, Jeong JO. Intracoronary catheter aspiration can be an adequate option in patients with acute myocardial infarction caused by left atrial myxoma. J Cardiovasc Ultrasound. 2009;17(4):145-7.
8. Charles RG, Epstein EJ, Holt S, Coulshed N. Coronary embolism in valvular heart disease. Q J Med. 1982;51(202):147-61.
9. Box LC, Hanak V, Arciniegas JG. Dual coronary emboli in peripartum cardiomyopathy. Tex Heart Inst J. 2004;31(4):442-4.
10. Kiernan TJ, Flynn AM, Kearney P. Coronary embolism causing myocardial infarction in a patient with mechanical aortic valve prosthesis. Int J Cardiol. 2006;112(2):e14-6.
11. Hernandez F, Pombo M, Dalmau R, Andreu J, Alonso M, Albarran A, et al. Acute coronary embolism: angiographic diagnosis and treatment with primary angioplasty. Catheter Cardiovasc Interv. 2002;55(4):491-4.
12. Rifaie O, Nammas W. Coronary air embolism during mitral valvuloplasty. Acta Cardiol. 2011;66(5):665-7.
13. Braun S, Schrotter H, Reynen K, Schwencke C, Strasser RH. Myocardial infarction as complication of left atrial myxoma. Int J Cardiol. 2005;101(1):115-21.